Understanding shear-resisting mechanism in reinforced engineered cementitious composite (ECC) beams using distributed strain measurements

Gu, Dawei; Pan, Jinlong; Luković, Mladena

DOI
10.1016/j.engstruct.2025.119612

Publication date
2025

Document Version
Final published version

Published in
Engineering Structures

Engineering Structures 327 (2025) 119612

Contents lists available at ScienceDirect

Engineering Structures

journal homepage: www.elsevier.com/locate/engstruct

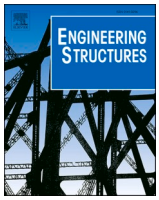

Understanding shear-resisting mechanism in reinforced engineered cementitious composite (ECC) beams using distributed strain measurements

Dawei Gu [a,b], Jinlong Pan [a,*], Mladena Luković [b]

[a] School of Civil Engineering, Southeast University, Nanjing 211189, China
[b] Faculty of Civil Engineering and Geosciences, Delft University of Technology, Delft 2600 AA, the Netherlands

ARTICLE INFO

Keywords:
Engineered cementitious composite (ECC)
Beam
Shear
Stirrup
Shear strength prediction model

ABSTRACT

Engineered cementitious composite (ECC) has been effectively applied in shear-critical structures due to its high ductility under tension and fiber bridging effect to resist crack opening and sliding. This study employed a novel monitoring system incorporating distributed strain gauges to investigate the shear resistance mechanism in reinforced ECC beams. The system enabled the measurement of full-length strain distribution along the stirrups and longitudinal reinforcement. By capturing stirrup strains precisely along the critical shear cracking path, the shear contributions from transverse reinforcement (V_s) and ECC matrix (V_c) could be accurately quantified. A total of 20 reinforced ECC beams were tested under shear, and the role of governing parameters (e.g., shear span-to-depth ratio, stirrup and longitudinal reinforcement ratio) was analysed. Based on the observed shear failure mechanism, a modified truss-strut model and a simplified equation for predicting shear strength are proposed for the shear design of reinforced ECC beams.

1. Introduction

Concrete has been the most widely used construction material in civil engineering due to its excellent compressive strength, durability, ease of production, and the widespread availability of its ingredients. However, its inherent brittleness and limited energy dissipation capacity can lead to significant damage or even structural collapse during earthquakes, resulting in the loss of property and lives [1]. To improve the ductility of concrete, a type of engineered cementitious composites (ECC) was developed [2]. By incorporating a high volume percentage (typically 1–2 %) of synthetic fibers and tailored fiber-matrix interface, ECC exhibits strain-hardening behavior under tension, characterized by the formation of multiple fine cracks, as illustrated in Fig. 1 [3,4]. Its ultimate tensile strain varies between 3 % and 12 %, which is 300–1200 times higher than that of traditional concrete [5]. Consequently, ECC exhibits ductile deformation similar to steel rather than brittle fracture during four-point bending, as demonstrated in Fig. 2, earning it the nickname “bendable concrete”. Substituting brittle concrete with ECC in key structural elements can significantly enhance the seismic performance of structure by increasing energy dissipation capacity [6–9], reducing story drifting [10] and/or preventing collapse [11].

Due to its high tensile ductility, ECC also exhibits outstanding shear resistance. Its shear strength can be up to twice that of conventional concrete, with unique ductile deformation characteristics [12]. In recent years, extensive experimental and analytical work has been conducted to understand the shear-resisting mechanism in ECC material, including the impressive shear test of Iosipescu beam by van Zijl [13], shear transfer under combined crack opening and sliding by Kanakubo et al. [14] and Wu et al. [15], and so on. Given its excellent shear resistance, ECC has been utilized in various shear-critical elements, such as coupling beams in high-rise structures to enhance seismic performance [16], beam-column joints [17,18], shear walls [19,20], shear strengthening of existing structures [21,22], etc. Reinforced ECC (R/ECC) elements and structures have demonstrated high shear strength, superior ductility, and effective energy dissipation [23–29].

Several shear strength prediction models for R/ECC members have been proposed, which can be categorized into two main types: (i) mechanics-based models, such as the truss-strut model [14,25,30,31] and modified compression-field theory [32], and (ii) empirical models [28,29]. Both types decompose the total shear resistance (V_u) into two components: the shear contribution from the ECC matrix (V_c), and the shear contribution from the stirrups (V_s), as illustrated in Fig. 3 and

* Corresponding author.
E-mail address: cejlpan@seu.edu.cn (J. Pan).

https://doi.org/10.1016/j.engstruct.2025.119612
Received 24 September 2024; Received in revised form 27 November 2024; Accepted 2 January 2025
Available online 15 January 2025

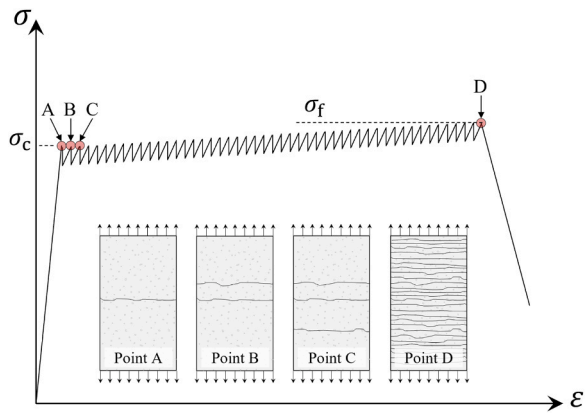

Fig. 1. Schematic stress-strain relationship of ECC under uniaxial tension.

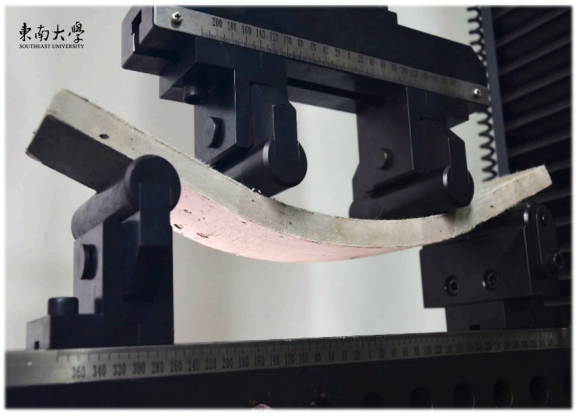

Fig. 2. Ductile deformation of ECC under four-point bending.

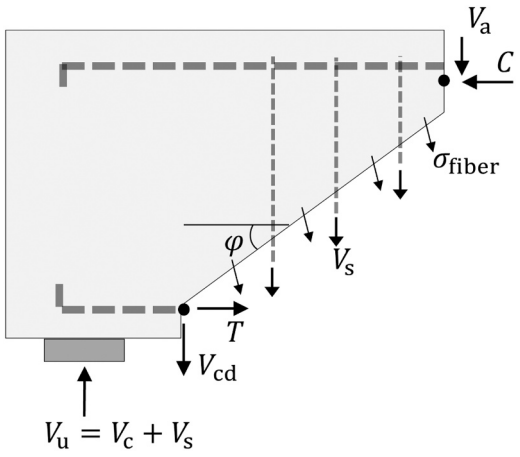

Fig. 3. Shear resistance components in R/ECC beams.

expressed by Eq. (1). Accurate quantification of V_c and V_s during shear tests is critical for developing and validating reliable shear design models for R/ECC members. Nevertheless, direct measurement of V_c poses significant challenges due to the complex interplay of mechanisms such as fiber bridging across shear cracks, the contribution of ECC in the shear-compression zone, and the dowel action of longitudinal reinforcement. A practical alternative is to measure V_s, with V_c determined by subtracting V_s from V_u. The stirrups' contribution to shear resistance (V_s) can be expressed as $\sum_1^n V_{si}$, where V_{si} is the tensile force in the i-th stirrup leg intersecting the critical shear crack, and n is the number of intersected stirrup legs. Therefore, accurately capturing stirrup strains along the critical shear cracking path is vital for determining V_s.

$$V_u = V_c + V_s = V_c + \sum_1^n V_{si} \quad (1)$$

Traditional methods often measure stirrup strain by attaching strain gauges at the stirrup's mid-height [25,26,33,34], as shown in Fig. 4(a). However, due to the bond between the stirrups and ECC, stirrup strain distribution can vary along the height of the beam. Consequently, mid-height measurements may not reflect the actual strain at the critical crack intersection. Alternatively, strain gauges can be attached along an assumed shear crack path [35,36], as illustrated in Fig. 4(b). Yet, due to the heterogeneity of ECC, accurately predicting the crack path before testing remains a challenge.

To address these limitations, a distributed strain gauging approach along the reinforcement is ideal, as depicted in Fig. 4(c) [37,39–41]. A promising approach involves dividing the stirrup into two halves to create internal cavities and attaching strain gauges continuously along the stirrup legs, a method demonstrated to be effective in a pilot experimental work [24]. As a follow-up to the work by Gu et al. [24], a total of 20 R/ECC beams were tested under shear to further evaluate the effects of shear span-to-depth ratio, stirrup ratio, and longitudinal reinforcement ratio on the shear strength components V_c and V_s. The existing shear strength prediction models for R/ECC were then systematically evaluated, and modifications to the mechanics-based truss-strut (or arch) model were proposed to establish a more accurate shear design methodology.

2. Experimental program

2.1. Beam design

A total of 20 R/ECC beams were fabricated for the shear test. The investigated parameters include stirrup ratio (ρ_t), longitudinal tensile reinforcement ratio (ρ_l) and shear span-to-effective depth ratio (a/d), as listed in Table 1. The geometric and reinforcement details of three typical beams with different shear span-to-effective depth ratios (a/d=2.0, 2.5, 3.0) are shown in Fig. 5. All beams had an ECC cover thickness of 20 mm. The distributed strain gauging scheme along reinforcement was employed only within the left span of each beam, while the right span was configured with closely spaced stirrups to prevent shear failure.

2.2. Distributed strain gauging system along reinforcement

A distributed strain gauging system was utilized to accurately measure the contribution of stirrups to the shear resistance of the beams. Strain gauges were embedded within the stirrup legs, allowing precise measurement of stirrup strain at the critical shear crack without disrupting the bond between the stirrups and the matrix. Steel reinforcement of grade HRB400 with a diameter of 12 mm was used to fabricate the stirrups through the following steps: (1) Screw threads were created at both ends of the straight rebars; (2) The rebars were then cut into two halves, and cavities with a depth of 1.5 mm and a width of 6 mm were machined into each half using Computer Numerical Control (CNC) techniques; (3) Five strain gauges were mounted inside each cavity along each half bar, resulting in a total of 10 strain gauges distributed along the length of each stirrup leg (Fig. 6(a)). Detailed layouts of the strain gauges are provided in Fig. 6(b); (4) The strain gauges were sealed with epoxy resin, and the cavities were filled with silicone sealant to prevent water infiltration during the ECC casting process; (5) The two half bars were re-joined using high-strength epoxy resin, with mechanical tightening rings fixed to enhance the bonding strength between the bars (Fig. 7(a)); (6) After 72 hours' healing, the rings were removed, and the stirrup leg fabrication was done. To avoid damaging the strain

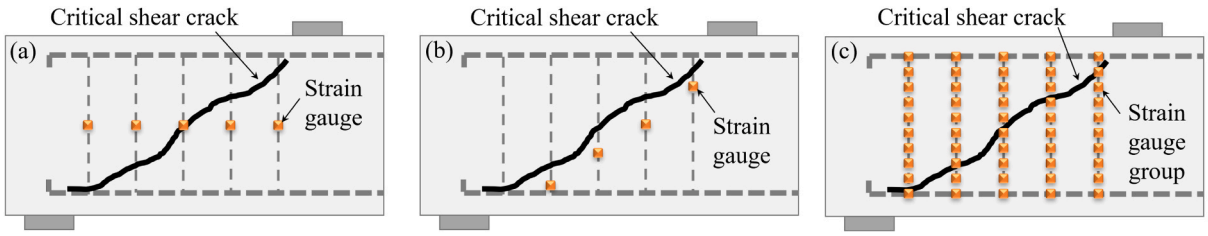

Fig. 4. Three schemes for measuring stirrup strains: (a) attaching strain gauges at the mid-height of the stirrup [25,26,28,34]; (b) attaching strain gauges along the predicted cracking path [35,36]; (c) attaching a set of strain gauges along the stirrup [24,37–39].

Table 1
Summary of tested beam specimens.

Specimen ID	a/d	Stirrup	Bottom reinforcement	Top reinforcement	ρ_l (%)	ρ_t (%)
SN4	2.0	–	4D22	3D22	2.1	0.00
SN5		–	5D22	3D22	2.6	0.00
SN6		–	6D22	3D22	3.2	0.00
SS6–250		D12@250	6D22	3D22	3.2	0.38
SS6–150		D12@150	6D22	3D22	3.2	0.63
SS6–100		D12@100	6D22	3D22	3.2	0.95
MN4	2.5	–	4D22	3D22	2.1	0.00
MN5		–	5D22	3D22	2.6	0.00
MN6		–	6D22	3D22	3.2	0.00
MS4–250		D12@250	4D22	3D22	2.1	0.38
MS5–250		D12@250	5D22	3D22	2.6	0.38
MS6–250		D12@250	6D22	3D22	3.2	0.38
MS6–150		D12@150	6D22	3D22	3.2	0.63
MS6–100		D12@100	6D22	3D22	3.2	0.95
LN4	3.0	–	4D22	3D22	2.1	0.00
LN5		–	5D22	3D22	2.6	0.00
LN6		–	6D22	3D22	3.2	0.00
LS6–250		D12@250	6D22	3D22	3.2	0.38
LS6–150		D12@150	6D22	3D22	3.2	0.63
LS6–100		D12@100	6D22	3D22	3.2	0.95

Notes: ρ_l = bottom (tensile) reinforcement ratio; ρ_t = stirrup ratio; a/d = shear span-to-effective depth ratio. For the specimen ID, the first letter 'S', 'M' and 'L' represent the short, medium and long beams with a/d = 2.0, 2.5 and 3.0, respectively; the second letter 'S' and 'N' represent the beams with stirrups and with no stirrups respectively; the third number '6', '5'and '4' represent the number of bottom (tensile) reinforcements; the fourth number '250', '150' and '100' represent the stirrup spacing distance (unit: mm).

gauges during welding, a prefabricated U-shaped bar with coupling rings, serving as connectors, was used (Fig. 7(b)). The two legs of the stirrup were then secured by the U-shaped connector, and a closed stirrup with distributed strain gauges embedded inside was done (Fig. 7(c)).

For the longitudinal reinforcement, steel bars of grade HRB600 with a diameter of 22 mm were used, and a similar strain gauging system was installed on all longitudinal rebars. Initially, a cavity with a depth of 4 mm and a width of 8 mm was machined on the side surface of the rebar, and ten strain gauges were installed inside this cavity, as shown in Fig. 8(a). To avoid disrupting the bond between the rebar and concrete, the cavity was placed in a rib-free section of the bar. Strain gauges were installed on half of the longitudinal reinforcement within the designed shear failure span. The layout and position of the strain gauges for different beams are shown in Fig. 8(b). Considering that the bending (dowel action) or buckling of longitudinal reinforcement can cause a strain gradient along the rebar section [40], the cavity with strain gauges was oriented towards the beam side to accurately measure the axial strain of the rebar, as illustrated in Fig. 9(a). The cavity was sealed with silicone sealant to protect the strain gauges, and steel plates with a thickness of 10 mm were used for anchoring longitudinal reinforcement, as shown in Fig. 9(b). After assembling the steel reinforcement cage, the ECC was cast from the side of the beam to facilitate vibration, as shown in Fig. 9(c).

2.3. Material preparation

The composition of ECC mixture is detailed in Table 2. The ECC incorporated short Polyvinyl Alcohol (PVA) fibers, specifically the RECS15 type developed by Kuraray Co., Ltd., with a length of 12 mm, a diameter of 40 μm, and a volume fraction of 2 %. According to the manufacturer, the tensile strength and Young's modulus of the fibers are 1560 MPa and 41 GPa, respectively. As ECC's ductility can be enhanced by reducing the fracture toughness and cracking strength of its cementitious matrix, cenosphere, as a by-product of fly ash, was incorporated into the ECC matrix [42]. Fig. 10 presents the SEM micrograph of the cenosphere within ECC, while Fig. 11 displays the cumulative percentage distribution of the raw material. For each beam, four standard dumbbell-shaped specimens were prepared to characterize the uniaxial tensile stress-strain behavior of ECC, following JC/T 2461–2018 [43] and JSCE-08 [44], as shown in Fig. 12(a) and (b). In addition, six cylinders with a diameter of 100 mm and a height of 200 mm for each beam were prepared to test the compressive strength following ASTM C 39 [45], and some of these specimens were selected to assess the uniaxial compressive stress-strain behavior of ECC, as shown in Fig. 12(c) and (d).

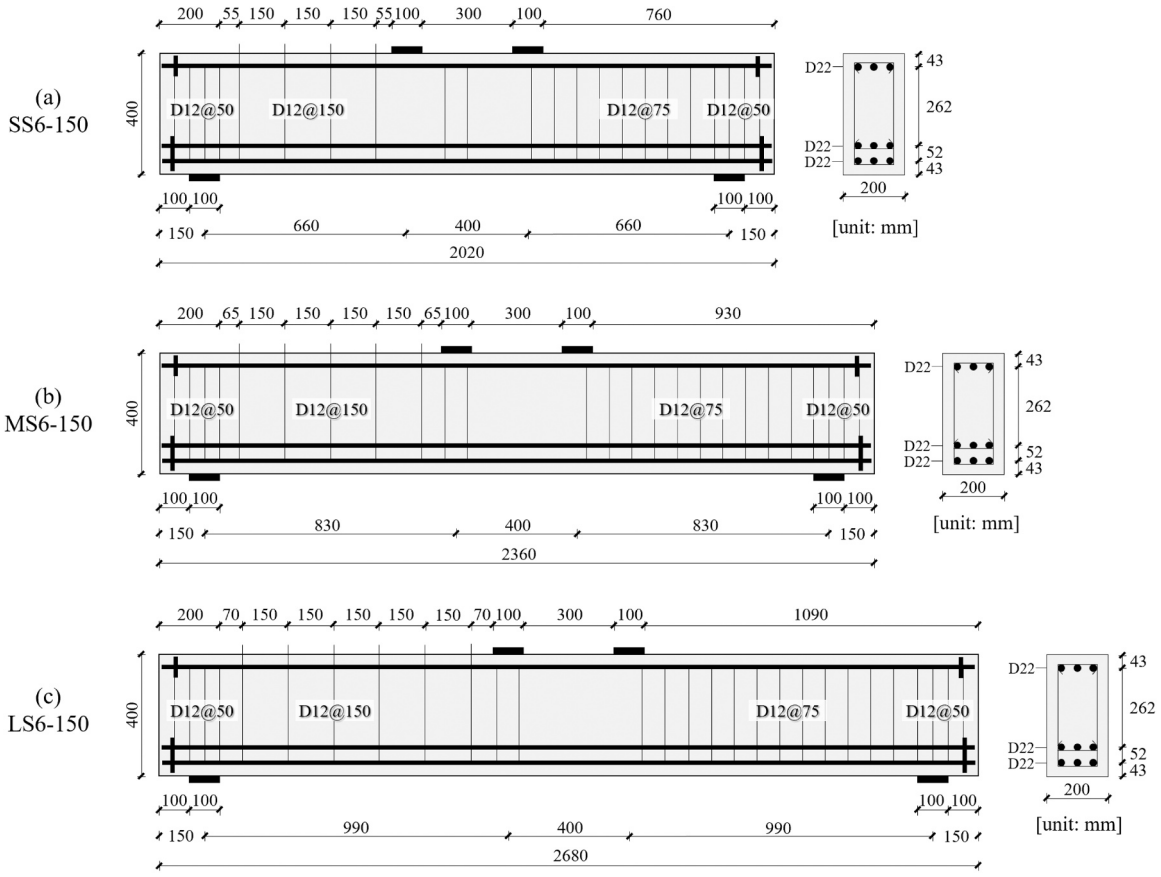

Fig. 5. Size and reinforcement details of selected beams: (a) SS6–150; (b) MS6–150; (c) LS6–150.

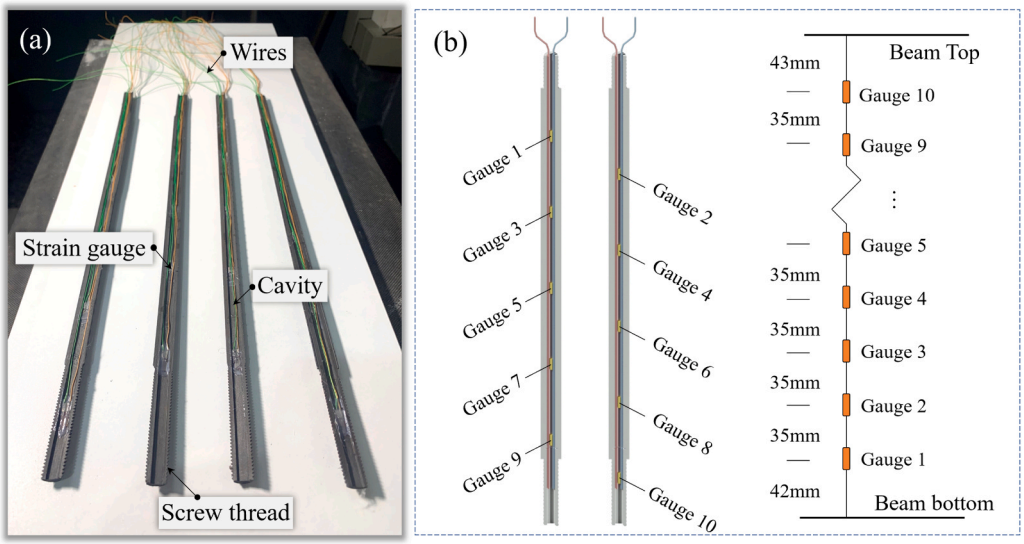

Fig. 6. Distributed strain gauges along the stirrup legs: (a) cutting the rebar into two halves, making cavities, and attaching strain gauges inside; (b) position of strain gauges relative to the beam dimensions.

2.4. Test setup and measurement program

The beam specimens were subjected to four-point bending through an electro-hydraulic servo testing system, as shown in Fig. 13. Steel plates with a thickness of 10 mm were used as anchorage for the stirrups on the top of the beam. A three-dimensional digital image correlation (3D-DIC) system was employed to capture the full-field strain in the left shear span. To monitor potential rotation of the mid-span cross-section due to the asymmetric configuration of stirrups, two linear variable displacement transducers (LVDTs) were positioned horizontally along the cross-section. Additionally, three LVDTs were employed to detect beam deflection and settlement at the supports. Strains and displacements from the strain gauges and LVDTs were recorded using multiple data logging systems with an acquisition frequency of 2 Hz. The loading

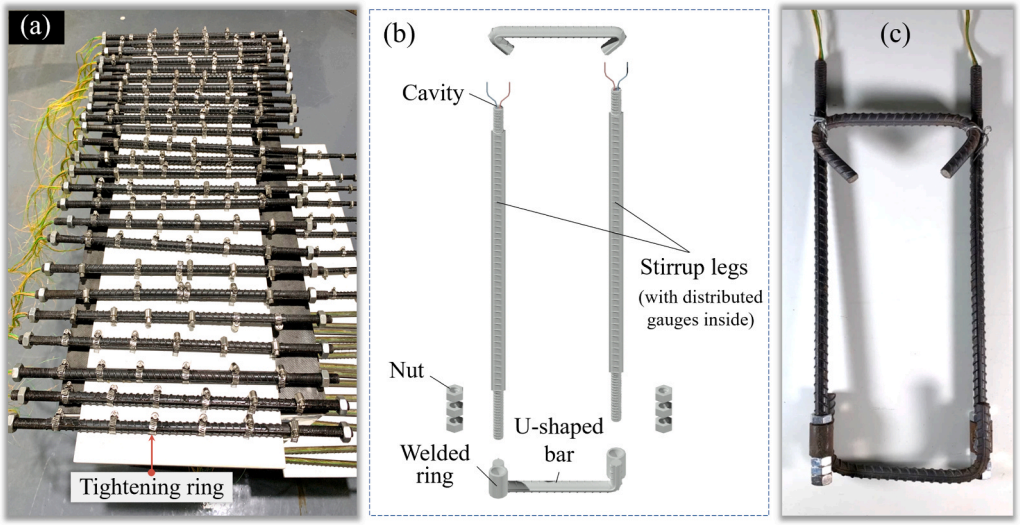

Fig. 7. Fabrication of closed stirrups: (a) recombination of the two half bars using tightening rings; (b) components of the closed stirrup; (c) assembly of the closed stirrup.

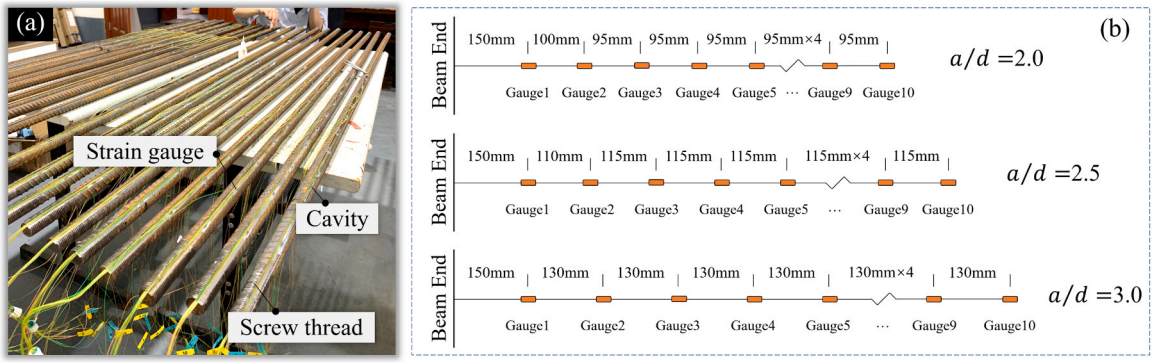

Fig. 8. Longitudinal reinforcement equipped with distributed strain gauges: (a) strain gauges and cavity on the rebar; (b) position of strain gauges relative to beam dimensions.

process was controlled by displacement at a rate of 0.4 mm/min.

3. Experimental results

3.1. Material tests

The reinforced ECC beams and the corresponding cylinders and dumbbell-shaped specimens, were tested at the same day. Table 3 summarizes the measured average compressive strength f_c', average nominal yielding strength f_{ty}, tensile strength f_{tu} and ultimate tensile strain ε_{tu} of ECC following their definition by JSCE-08 [44]. The results of all tests with respect to different testing ages are shown in Fig. 14.

As commonly observed for fiber reinforced materials, there is significant variability in both the tensile and compressive strengths of ECC (Fig. 14(a)), with particularly high variability in its strain capacity under tension (Fig. 14(b)). The mechanical behavior of ECC is notably time-dependent. With increased curing age, ECC generally exhibits higher compressive and first-cracking strengths but lower tensile strain capacity, attributed to the ongoing hydration of the cementitious matrix [5,46]. Selected typical stress-strain relationships for uniaxial compression and tension are presented in Fig. 15. Although it is important to consider the substantial scatter in ECC material properties, a normalized shear strength factor will be introduced in a later section to eliminate the effect of material strength when evaluating the shear-carrying capacity of the beam.

The original, re-joined rebars (used as stirrup legs) and grooved rebars (used as longitudinal reinforcement) were tested under uniaxial tension, and the stress-strain curves are plotted in Fig. 16. Comparison of the different types of rebars shows that the cutting or grooving process did not significantly affect their mechanical properties. The yielding strengths of the HRB400 rebar (used as stirrups) and the HRB600 rebar (used as longitudinal reinforcement) were measured to be 440 MPa and 635 MPa, respectively.

3.2. Failure modes and shear force-deflection response

All the beam specimens failed in shear except MS6–100, LS6–150 and LS6–100, which reached flexural capacity prior to shear failure, as shown in Fig. 17. Although the shear span-to-effective depth ratio varied from 2.0 to 3.0, the shear-compression failure tended to be the dominant failure mode in those beams failing in shear, i.e., the shear-carrying capacity was reached due to the crushing of ECC in shear-compression zone beneath the loading plate.

The shear force-deflection curves for all tested beams are plotted in Fig. 18(a) to (d), and a comparison is made between R/ECC and reference R/C beams (specimen details can be found in [47]) as shown in Fig. 18(e). From the initial loading to the peak load, almost linear shear force-deflection behavior could be found in most beams without obvious stiffness degradation, although multiple cracking took place during the loading. This differs from the conventional R/C beam, in which the

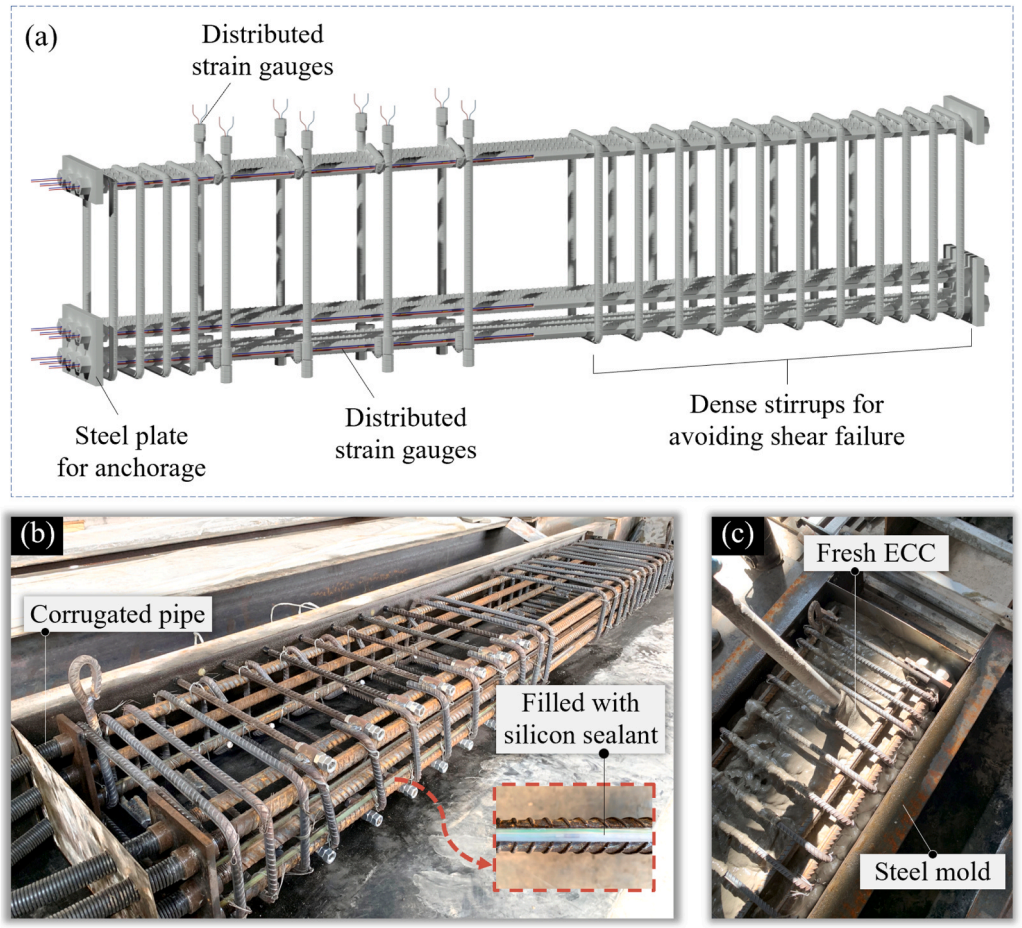

Fig. 9. Beam fabrication: (a) detailed view of the steel reinforcement cage; (b) cavity filled with silicon sealant; (c) ECC casting.

Table 2
Mixture proportions of ECC (kg/m^3).

Cement (P.O 42.5)	Fly ash (grade II)	Cenosphere	Silica fume	Quartz powder	Water	PVA fiber	Superplasticizer	Hypromellose
426	647	162	43	256	332	26.8	1.6	0.5

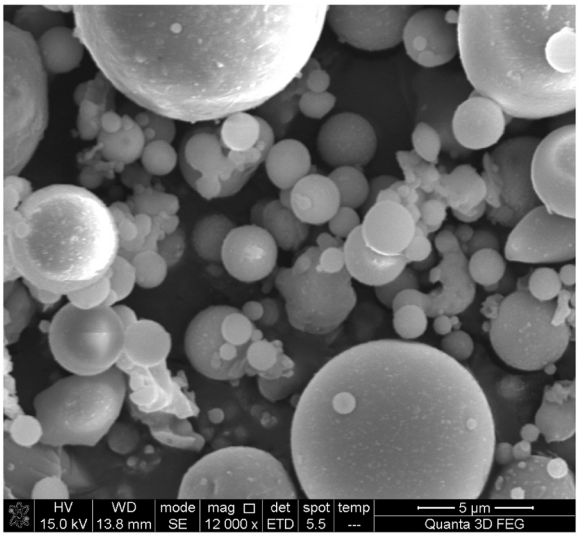

Fig. 10. SEM micrographs of cenosphere incorporated in ECC.

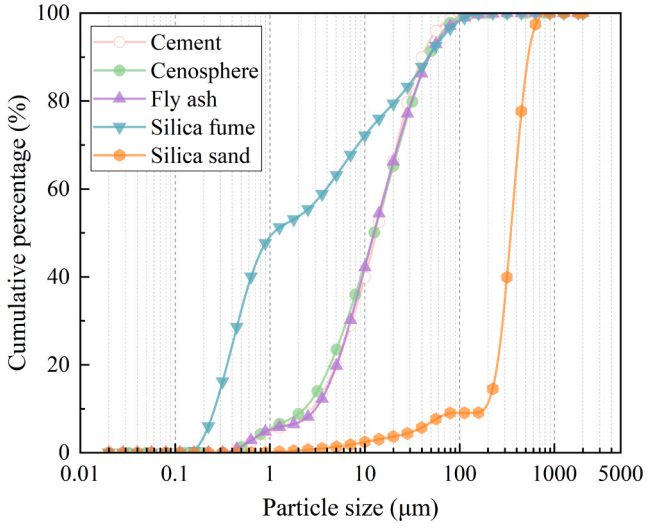

Fig. 11. Cumulative percentage distribution of ECC's raw material.

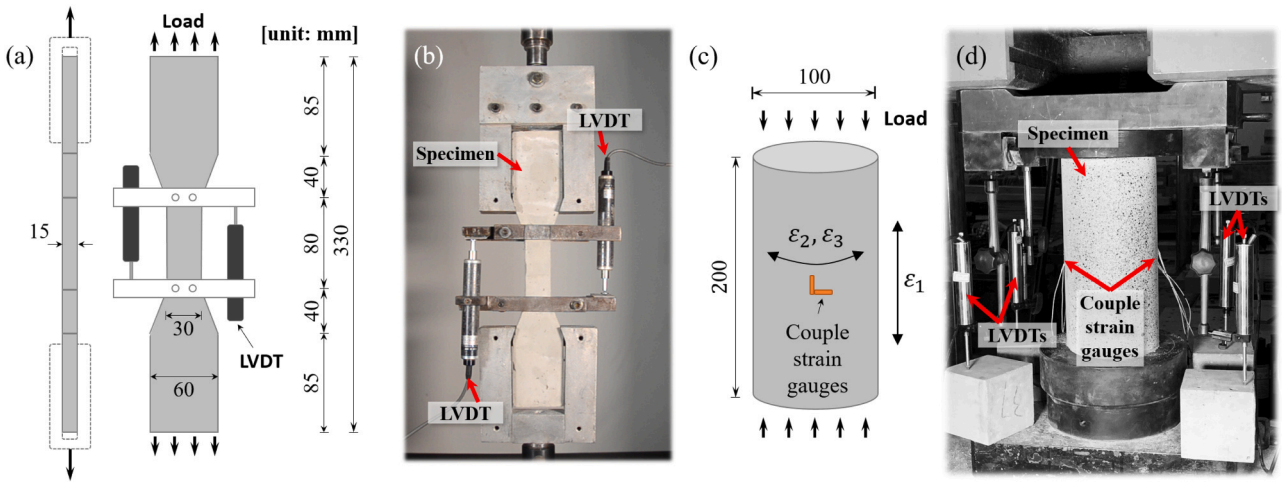

Fig. 12. Material test scheme: (a) specimen size of uniaxial tension test; (b) test setup of uniaxial tension test; (c) specimen size of uniaxial compression test; (d) test setup of uniaxial compression test.

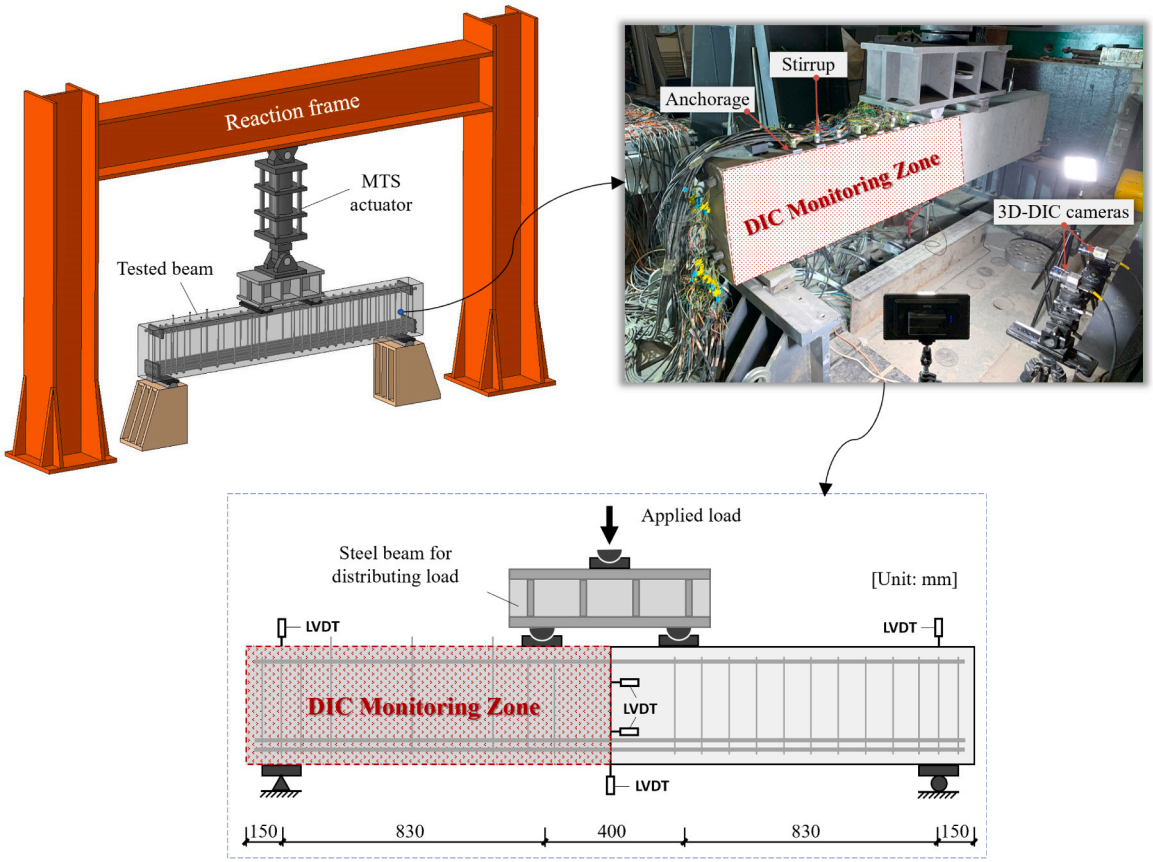

Fig. 13. Four-point bending test setup of the beam.

initial cracking can cause significant stiffness loss. For the beams SS6–100, MS4–250 and LN4, it is interesting to find a ductile yielding phase before the peak load, instead of a typical brittle shear failure. Such failure mode could happen when the longitudinal reinforcement yielded before reaching the beam's ultimate shear strength, which was somewhat lower than the ultimate flexural capacity of the beam. In other words, it was a special transitional failure mode between the flexure and shear (named as 'flexure-shear failure' in Table 3), when the longitudinal reinforcement yielded but the peak load was reached due to a lack of shear resistance.

3.3. Crack propagation

Using 3D-DIC, the full-field displacement of the beam could be obtained, and the principal strain of selected beams was further analysed and plotted in Fig. 19. Then, the cracks in ECC could be identified as the region with concentrated tensile strain [48,49]. Due to camera deviations, some images exhibited unrealistically high strain values at the corners or edges of the beam (e.g., SN6, SS6–250 and LS6–150). Nevertheless, the propagation of shear cracks within specific areas could still be distinguished.

Table 3
Summary of beams and test results.

Specimen	a/d	Testing age (days)	f'_c (MPa)	f_{ty} (MPa)	f_{tu} (MPa)	ε_{tu} (%)	ρ_l (%)	ρ_t (%)	V_u (kN)	v_u (MPa)	Failure mode
SN4	2.0	123	54.7	5.8	7.5	3.6	2.1	0.00	295.3	4.5	Shear
SN5		120	56.7	6.5	8.0	3.2	2.6	0.00	344.9	5.2	Shear
SN6		110	55.8	5.6	7.9	3.8	3.2	0.00	377.9	5.7	Shear
SS6–250		108	54.8	6.9	8.0	2.9	3.2	0.38	477.0	7.2	Shear
SS6–150		100	45.3	5.4	7.0	4.3	3.2	0.63	557.9	8.4	Shear
SS6–100		104	45.1	5.2	7.2	4.5	3.2	0.95	628.0	9.5	F-S
MN4	2.5	106	67.1	6.9	8.1	1.9	2.1	0.00	286.4	4.3	Shear
MN5		107	61.7	6.5	8.2	2.6	2.6	0.00	295.3	4.5	Shear
MN6		85	56.4	6.4	8.0	3.5	3.2	0.00	289.5	4.4	Shear
MS4–250		98	54.1	5.8	7.4	2.6	2.1	0.38	385.5	5.8	F-S
MS5–250		95	54.3	5.9	7.6	3.2	2.6	0.38	404.0	6.1	Shear
MS6–250		100	54.7	6.1	7.5	3.8	3.2	0.38	421.4	6.4	Shear
MS6–150		91	51.9	5.9	7.0	3.5	3.2	0.63	462.4	7.0	Shear
MS6–100		101	51.0	4.7	6.6	3.6	3.2	0.95	524.3	7.9	Flexure
LN4	3.0	127	73.9	7.2	8.0	1.5	2.1	0.00	302.4	4.6	F-S
LN5		125	58.4	6.2	7.7	3.1	2.6	0.00	261.4	3.9	Shear
LN6		113	59.1	6.4	7.6	2.8	3.2	0.00	302.0	4.6	Shear
LS6–250		112	57.0	5.3	7.4	3.1	3.2	0.38	365.7	5.5	Shear
LS6–150		101	44.8	5.2	6.5	4.2	3.2	0.63	421.9	6.4	Flexure
LS6–100		101	45.2	5.5	6.9	4.2	3.2	0.95	427.2	6.5	Flexure

Notes: a/d = shear span-to-effective depth ratio; f'_c = compressive strength; f_{ty} = nominal tensile yielding strength (first cracking strength); f_{tu} = tensile strength; ε_{tu} = ultimate tensile strain; ρ_l = bottom (tensile) reinforcement ratio; ρ_t = stirrup ratio; V_u = shear-carrying capacity; v_u = nominal shear strength; F-S represents the flexure-shear failure.

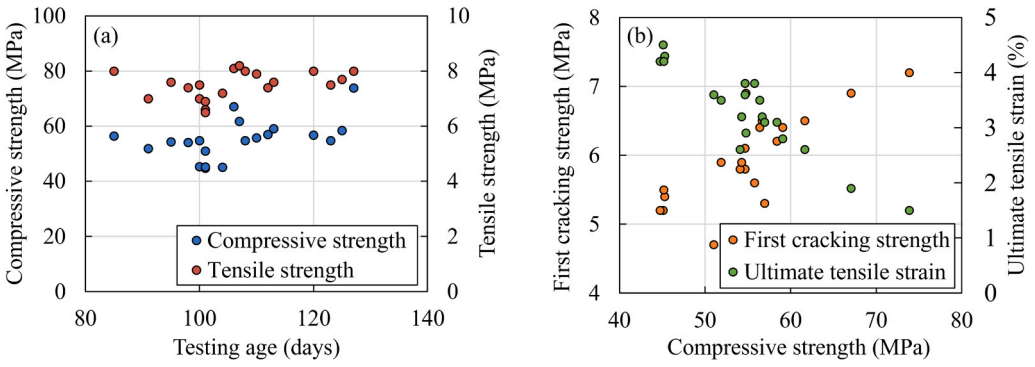

Fig. 14. Material test results of ECC: (a) compressive strength and tensile strength with respect to testing ages; (b) first cracking strength and ultimate tensile strain with respect to compressive strength.

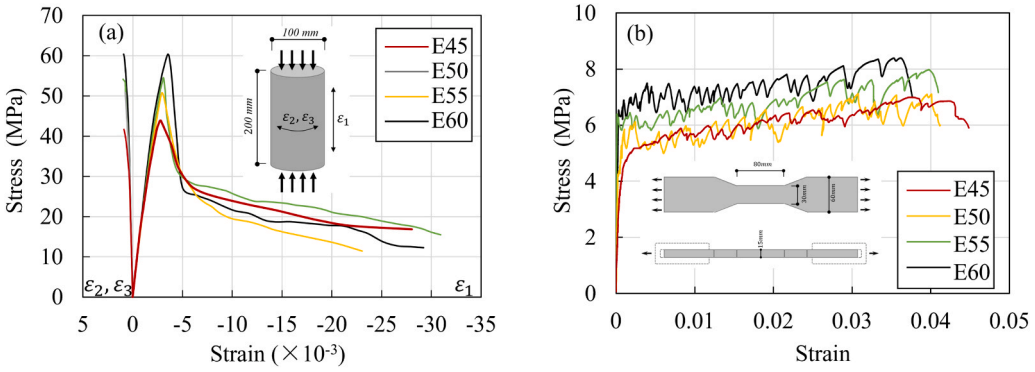

Fig. 15. Tested stress-strain curves of ECC under uniaxial: (a) compression; (b) tension (E45, E50, E55 and E60 represent material samples of different compressive strength, which correspond to the beam specimens LS6–150, MS6–100, SN6 and LN6 respectively).

In consistency with the observation in ECC under direct tension, all tested R/ECC beams exhibited multi-shear cracking behavior. To exhibit the crack propagation at different loading levels, the nominal shear stress v ($v = V/bd$) is given besides the strain spectrum in Fig. 19. For all beams, one or more vertical flexural cracks appeared at the beam bottom near the mid-span when v reached 1.0 MPa. As v increased to 2.0 MPa, additional flexural cracks formed with some beginning to rotate toward the loading plate, indicating the initial formation of shear cracks. At v

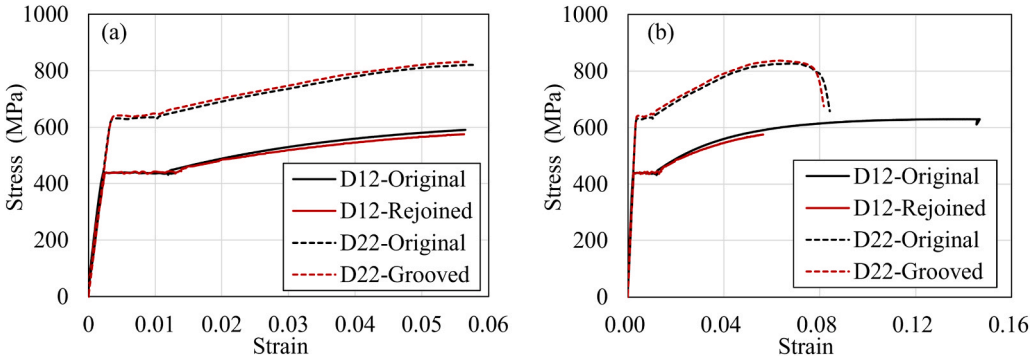

Fig. 16. Tested stress-strain relationship of rebars under uniaxial tension: (a) strain less than 0.06; (b) full curve until rebar fracture.

values of 3.0 and 4.0 MPa, plenty of diagonal shear cracks generated, and shear crack localization was observed in beams without stirrups (e.g., SN6, MN6, LN5). Before v reached 5.0 MPa, ultimate shear failure happened in the beam MN6 and LN5, whereas the other beams could still sustain the increasing load. In general, beams with higher stirrup ratio or lower shear span-to-depth ratio exhibited higher shear strength and steeper shear crack, as shown in Fig. 17 and Fig. 19. Differently, for the 'L'-series beams with highest shear span-to-depth ratio, splitting crack formed along the bottom rebars near the peak load, indicating the failure of rebars' dowel action. When reaching the peak load, localization of one or more shear cracks happened in all beams, although most cracks kept small width.

4. Discussion

4.1. Tension-shifting, anchoring, and buckling of longitudinal reinforcement

The longitudinal reinforcement's strain distribution in selected beams is shown in Fig. 20 and Fig. 21, using the distributed strain gauging system detailed in Fig. 8. The reinforcement along the top layer (in compression), bottom inner layer (in tension) and bottom outer layer (in tension) is denoted by "LC", "LT-Inner" and "LT-Outer" respectively, and the strain data shown in Fig. 20 and Fig. 21 are an average of three reinforcement at the same layer. Different curves correspond to varying loading levels, namely 20 %, 40 %, 60 %, 80 % and 100 % of the peak load.

At the initial loading stage (20 % of the peak load), the strain distribution along the reinforcement closely followed the bending moment diagram of beam. However, as the load increased, strain concentration developed where shear cracks intersected the bottom reinforcement. This effect became more pronounced as the peak load approached, with concentrated strain values even surpassing those in regions of pure bending, as observed in Fig. 20(c), (e) and Fig. 21(c), (i). To interpret the underlying mechanism, Fig. 22 illustrates the force equilibrium of a free body after shear cracking. Once the critical shear crack forms, the shear force previously resisted by the uncracked section B-B' redistributes to the shear-compression zone B'-C, significantly increasing the normal and shear stress there. Simultaneously, the tensile force in the bottom reinforcement F_t along section A-A' increases abruptly, as it becomes governed by the higher bending moment of section B-B', rather than A-A' (assuming no shear transfer occurs along the critical shear crack). This phenomenon, known as tension-shifting effect [50], indicates that the classical Euler–Bernoulli beam theory's assumption of 'plane sections remaining plane' no longer applies [51]. The tension-shifting effect also led to increased anchoring force in the reinforcement; for instance, Fig. 20 shows high tensile strain at the support where the bending moment should theoretically be zero.

When configured with stirrups, the strain distribution along the longitudinal reinforcement became more uniform, and the anchoring force was reduced, as shown in Fig. 21. It gave evidence that the stirrup could effectively enhance the shear transfer along the diagonal crack, which helped mitigate the tension-shifting effect. Furthermore, the stirrup could provide additional confinement and enhance the bond between reinforcement and ECC, as indicated in [52,53]. Therefore, more shear stress could be transferred along the longitudinal reinforcement and the anchoring force could be further reduced. However, still somewhat high reinforcement strain was found at the support for the beams SS6–250 and MS6–250 which had relatively short shear span but high load carrying capacity, as shown in Fig. 21(c) and (f). This highlights the importance of effective anchorage for longitudinal reinforcement, especially in shear-critical R/ECC short beams. As for the longitudinal compressive reinforcement along the beam top, large tensile strains were detected near the peak load in some specimens (e.g., SN6 and MN6), as shown in Fig. 20(a) and (d), indicating buckling and bending of the top reinforcement. Such phenomenon was almost avoided in beams with stirrups, as shown in Fig. 21(a), (d) and (g), when almost perfect confinement was provided.

4.2. Non-uniformly distributed strain along stirrups

The position of the stirrup leg which firstly yielded in selected beams (SS6–250, MS6–250, LS6–250 and MS6–150 with varying shear span-to-depth ratios or stirrup ratios) is illustrated in Fig. 23, while the strain development of these stirrup legs is shown in Fig. 24.

At the initial loading stage, minimal strain was detected until the formation of shear cracks. In beams with higher shear span-to-depth ratio, the stirrup strain was activated earlier and grew faster with the load increase, revealing more rapid shear crack propagation. As a result, the stirrup in more slender beams yielded earlier, as demonstrated in Fig. 24(a), (b) and (d). The strain at the mid-height of the stirrups (SG5 and SG6) is emphasized in Fig. 24. Obviously, the initial yielding did not always take place at the stirrup's mid-height.

The strain distribution along stirrups in four selected beams (SS6–250, MS6–250, MS6–150, and LS6–250) under various loading levels is shown in Fig. 25. The strain data presented represent the average of the front and back stirrup legs, with the stirrup positions (row numbers) for each beam illustrated in Fig. 17. At 80 % of the ultimate load (V_u), most stirrups had not yet yielded, indicating a synergistic deformation behavior between the steel reinforcement and the ECC matrix. At the peak load, the stirrup strain increased significantly due to yielding, and the critical shear crack almost simultaneously formed along which the fiber bridging failed. All stirrups exhibited non-uniformly distributed strain along the beam's height, with strain concentrations typically located where cracks intersected the stirrups. Besides, two or more strain peaks were observed along the stirrups, as one stirrup leg may intersect multiple diagonal cracks, as depicted in Fig. 25 (a), (d), (f), (i), (l), (m) and (n). It is also noteworthy that the stirrups did not always yield along the critical shear crack at peak load, particularly near crack tips. For example, in stirrup row 1 of beams MS6–250 and

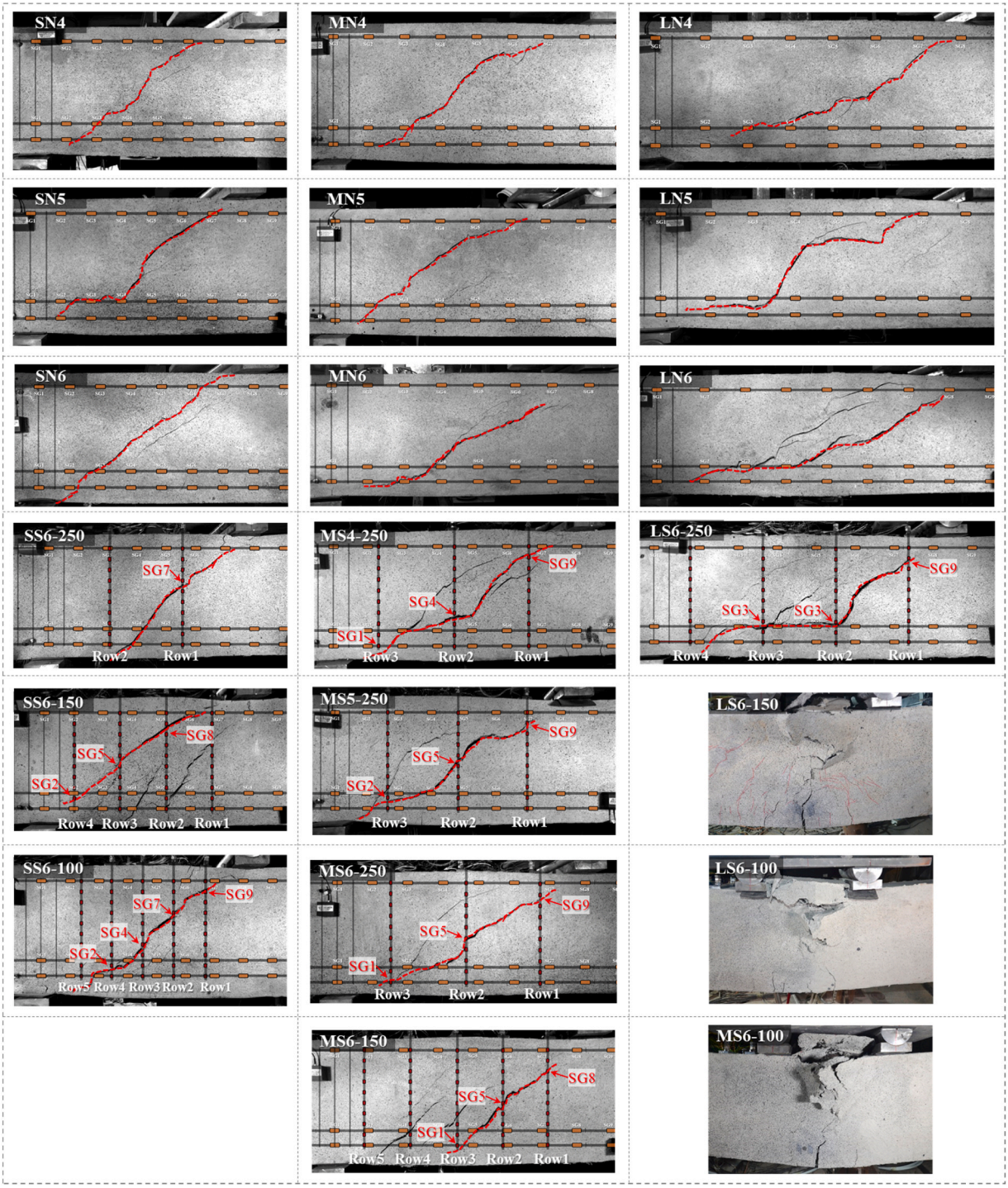

Fig. 17. Crack patterns at the ultimate failure of beams (the red dashed lines represent the critical shear crack, the tag "SG" represents the strain gauges within stirrups which intersected the critical shear crack).

LS6–250, the strain gauge point SG9 did not indicate yielding (Fig. 25 (c) and (k)). Therefore, evaluating V_s by summing the yielding forces of all stirrups within the critical shear cracking path could cause an overestimation of the stirrup contribution.

4.3. Quantification of shear strength components: V_s and V_c

With the measured strain distribution along the stirrup legs, the strain at the critical shear crack was determined. Using the tested stress-strain relationship from Fig. 16, the corresponding stirrup stress (σ) at the gauging points was calculated from the measured strain (ε). The tensile force of the i-th stirrup leg, V_{si}, was then calculated as $\sigma \bullet A_s$, where A_s represents the cross-section area of the stirrup leg (the cavity's area should be deducted). By summing the V_{si} values for all stirrup legs crossed by the critical shear crack, the shear contribution from stirrups, V_s, was obtained. Assuming that the calculated V_s was sufficiently accurate based on the measured distributed strain along stirrups, the shear contribution of concrete, V_c, was determined by subtracting V_s from V_u. The variations in V_c and V_s for the beams with stirrups that failed in shear are separately shown in Fig. 26.

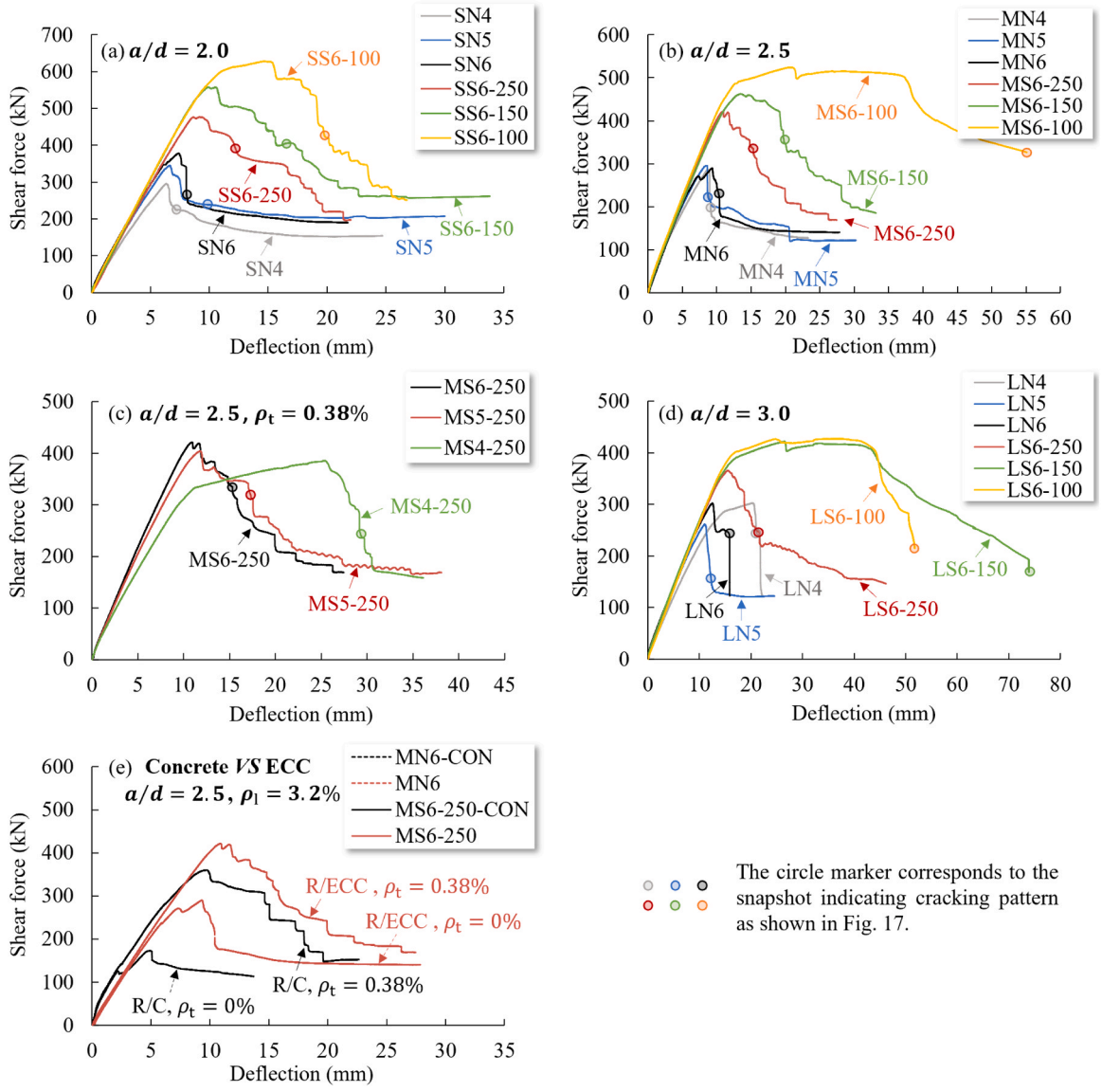

Fig. 18. Shear force-deflection curve of R/ECC beams: (a) a/d = 2.0; (b) a/d = 2.5; (c) a/d = 2.5 and ρ_t = 0.38%; (d) a/d = 3.0; (e) comparison between R/ECC beams and reference R/C beams.

For all R/ECC beams, the shear force was carried solely by V_c before the initial shear cracking, after which the stirrups came into work and V_s was activated. Different from conventional concrete [24,37], V_c in R/ECC beams showed no reduction when the initial crack occurred. Instead, it continued to increase until the peak load was reached (or a bit earlier). This indicates that the common assumption in ACI 318–19 [54] – that V_c equals the initial shear cracking force V_{cr} – is not applicable for R/ECC beams. Besides, V_c reached its peak resistance almost simultaneously or a little bit earlier than V_u, whereas V_s could remain constant or even increase further. The final failure in the beams resulted from the crushing of ECC beneath the loading plates, and most stirrups along the critical shear cracks did not fully yield.

To eliminate the effect of ECC's compressive strength f_c' when evaluating V_c of R/ECC beams, a dimensionless factor $V_c/f_c'bd$ is used, as shown in Fig. 27. With increasing shear span-to-depth ratio, the arch action diminishes, and beam action becomes more dominant, leading to a noticeable reduction in V_c. This observation aligns with previous findings by [55]. Conversely, increasing the stirrup ratio had limited influence on V_c in shorter beams (a/d = 2.0), but caused obvious decrease in V_c for more slender beams ($a/d \geq 2.5$). Fig. 28 compares V_s across beams that failed in shear. A higher V_s was consistently observed in beams with a higher stirrup ratio ρ_t. Nevertheless, this does not always mean that more stirrups were crossed by the critical shear crack. For instance, in beams MS6–250 (ρ_t = 0.38%) and MS6–150 (ρ_t = 0.63%), despite MS6–150 having more stirrups, it exhibited a steeper critical shear crack (as shown in Fig. 17), with the same number of stirrups crossed as in MS6–250. However, the stirrups in MS6–250 did not fully yield, resulting in a higher V_s in MS6–150. This demonstrates that both the number of activated stirrups and their stress levels influence V_s. As for the longitudinal reinforcement ratio, beams with higher ρ_l always showed higher V_c.

4.4. *Efficiency factor of stirrups*

When checking the stirrup strain, it was observed that some stirrups intersected by the critical shear crack did not yield when the beams reached their shear-carrying capacity, which indicates that the stirrup strength was not fully utilized. To evaluate the extent of stirrup utilization, an efficiency factor k is introduced, defined as

Fig. 19. Shear crack propagation in selected beams (left shear span) captured by 3D-DIC system.

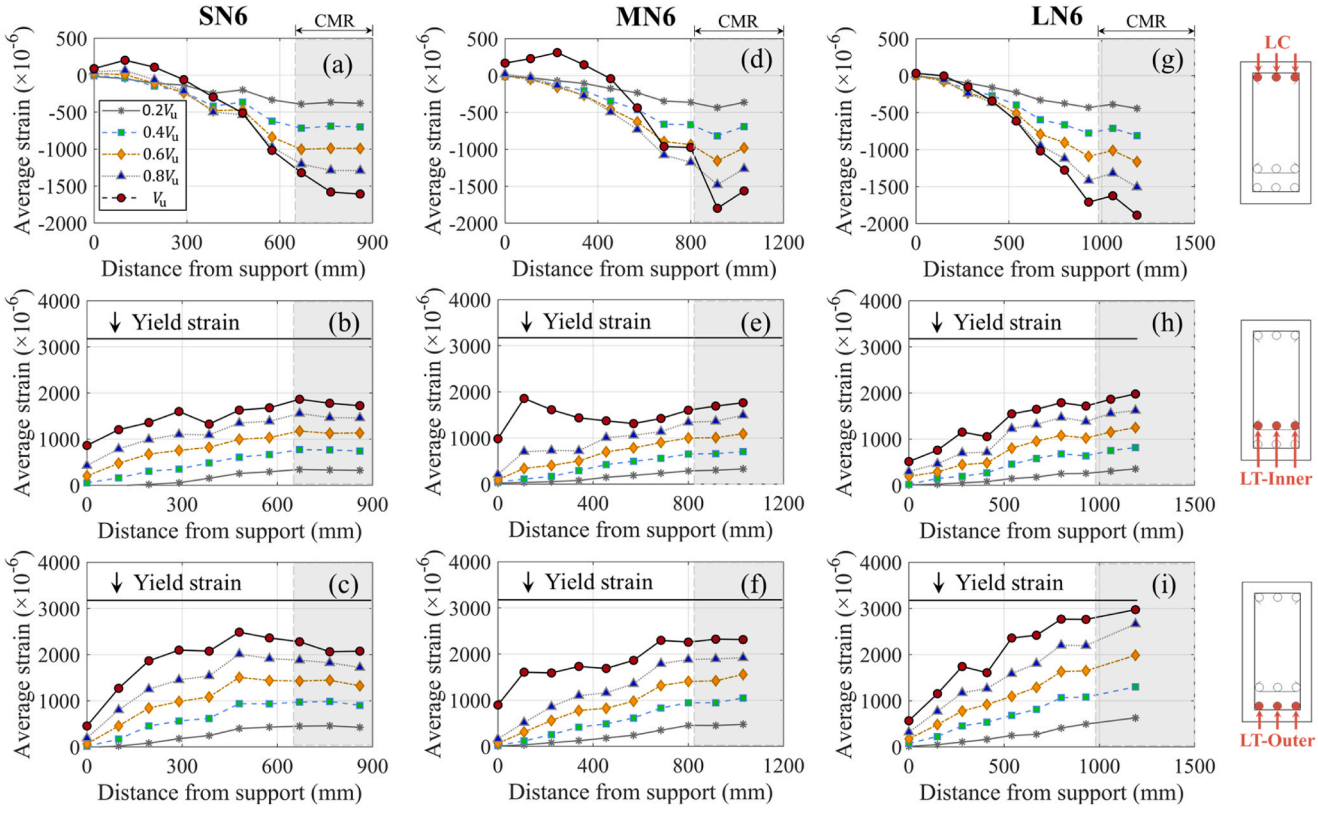

Fig. 20. Longitudinal reinforcement's strain distribution in selected beams without stirrups at selecting loading levels: (a) LC in SN6; (b) LT-Inner in SN6; (c) LT-Outer in SN6; (d) LC in MN6; (e) LT-Inner in MN6; (f) LT-Outer in MN6; (g) LC in LN6; (h) LT-Inner in LN6; (i) LT-Outer in LN6 (LC represents longitudinal compressive reinforcement, LT-Inner represents longitudinal tensile reinforcement at the inner layer, LT-Outer represents longitudinal tensile reinforcement at the outer layer, CMR represents the constant moment region).

$$k = \frac{f_{v,aver}}{f_{yv}} \tag{2}$$

where $f_{v,aver}$ is the average of stirrup stress at the critical shear crack and f_{yv} is the stirrup yield strength. It should be noted that $f_{v,aver}$ only concerns the stirrup stress at the critical shear crack, and does not refer to the average stress of all gauging points along a particular stirrup. The efficiency factors of stirrups (k) for the beams failing in shear are listed in Table 4. It is evident that the stirrups intersected by the critical shear crack did not fully yield in most beams, yet all exhibited an efficiency factor k higher than 0.8. Notably, the beam SS6–250 even demonstrated a k value exceeding 1.0, indicating that the stirrups had entered the

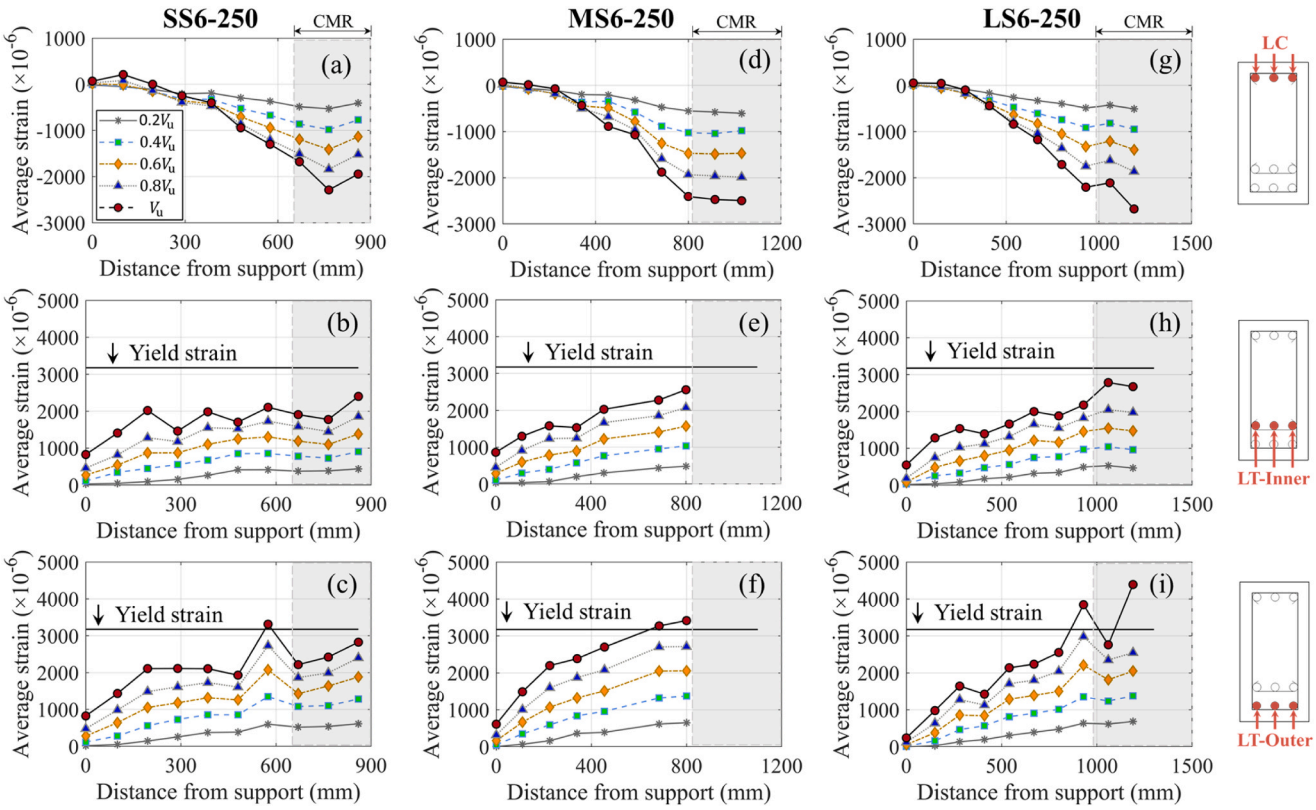

Fig. 21. Longitudinal reinforcement's strain distribution in selected beams with stirrups: (a) LC in SS6–250; (b) LT-Inner in SS6–250; (c) LT-Outer in SS6–250; (d) LC in MS6–250; (e) LT-Inner in MS6–250; (f) LT-Outer in MS6–250; (g) LC in LS6–250; (h) LT-Inner in LS6–250; (i) LT-Outer in LS6–250 (LC represents longitudinal compressive reinforcement, LT-Inner represents longitudinal tensile reinforcement at the inner layer, LT-Outer represents longitudinal tensile reinforcement at the outer layer, CMR represents the constant moment region).

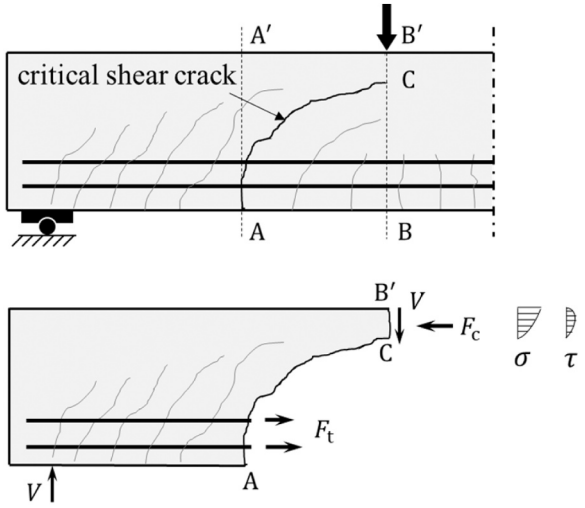

Fig. 22. Schematic diagram for tension-shifting effect after shear cracking.

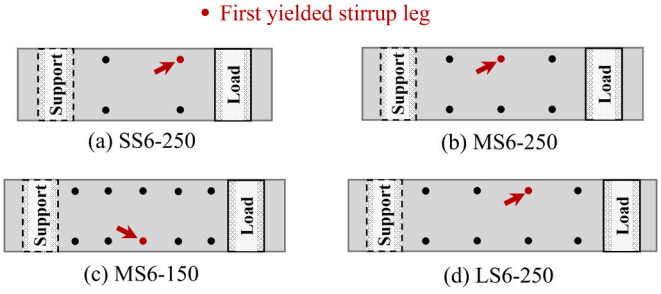

Fig. 23. First yielded stirrup leg's position (view from the beam's top) in the beam (a) SS6–250; (b) MS6–250; (c) MS6–150; (d) LS6–250.

tension-hardening phase. It is worth noting that, despite two rows of stirrups being arranged along the shear span of SS6–250 (as shown in Fig. 17), only one row was crossed by the critical shear crack. This observation suggests that not only the stirrup ratio but also the position of stirrups can significantly influence the shear contribution V_s. To avoid overestimating V_s in the shear design of reinforced concrete, Kim and Laskar et al. [56–58] recommended considering the number of activated stirrups as $(L_c/s)-1$ (with a local view at the free body diagram in Fig. 3), where L_c is the horizontal projection length of the critical shear crack and s is the stirrup spacing distance. However, this this conservative approach underestimates $V_s$for most R/ECC beams in this test, as it does not accurately account for the actual contribution of the stirrups.

4.5. Evaluation of existing shear strength prediction models

In this section, the test results are evaluated using five different shear strength prediction models for reinforced ECC beams proposed by various researchers and codes, as summarized in Table 5. The China specification T/CECS 1212–2022 [30], Kanakubo's model [14,31] and the author's proposed truss-strut model in previous research [25] all adopted a kind of mechanics-based shear strength model, which divided the shear resistance of R/ECC beams into two parts: truss action (including the fiber bridging and stirrup contribution) and strut action (shear force directly transferred by the ECC strut). The shear-resisting contribution from the residual tensile stress ($\mu_t f_{tu}$) along the critical

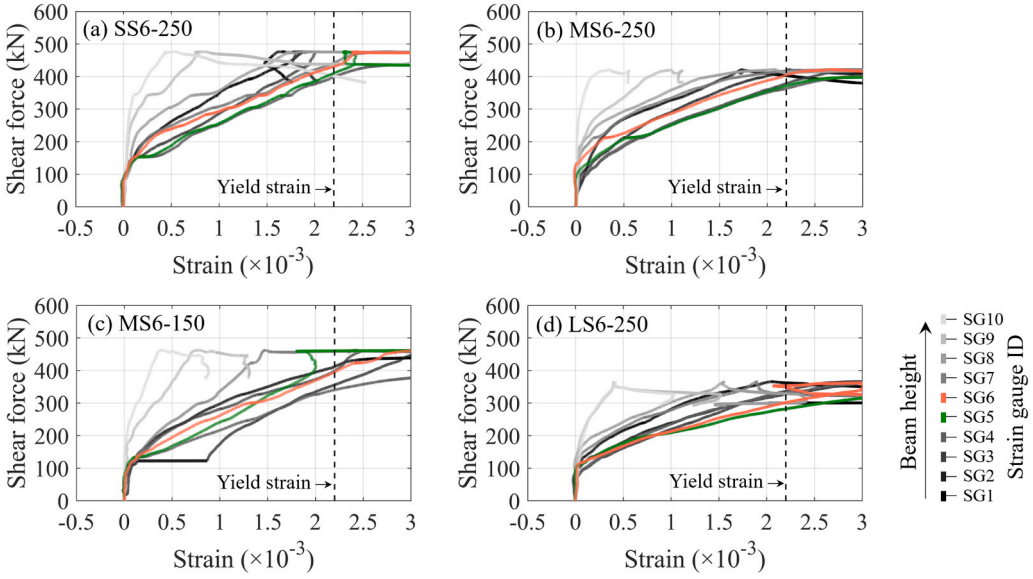

Fig. 24. Strain development of first yielded stirrup leg in the beam (a) SS6–250; (b) MS6–250; (c) MS6–150; (d) LS6–250.

shear crack is considered in all three models, where f_{tu} is the tensile strength of ECC and μ_t represents the reduction factor considering the localization of critical shear crack.

The V_c, V_s and V_u are separately calculated based on different models and compared with the experimental results, as listed in Table 6. All five models overestimate V_c to a certain extent (25 %~136 %). This discrepancy may result from the overestimation of shear-resisting contribution from residual tensile stress along the critical shear crack ($\mu_t f_{tu}$). According to a regression analysis [25], the tensile stress reduction factor (μ_t) decreases as the shear span-to-depth ratio increases, and the slender beams ($a/d \geq 2.5$) would have μ_t even lower than 0.2. Moreover, the crack kinematics analysis in [59] demonstrates that the critical shear crack width in R/ECC beam can exceed 2.0 mm before reaching the beam's shear strength. This suggests that fiber bridging across the critical shear crack is nearly exhausted when the slender beam reaches its shear-carrying capacity, and the residual tensile stress contribution should not be overestimated when evaluating shear strength components.

As for V_s, three of the evaluated models [30,34,44] show obvious underestimation (27 %~36 %) since they all assume the inclined angle of the critical shear crack (φ) to be 45°, which is steeper than the measured ones in tests. When taking φ as a variable, the truss-strut model [25] provides a more accurate estimation of V_s (average $V_{s,pre}/V_{s,exp} = 0.94$), but Kanakubo's model [14,31] makes distinct overestimation (average $V_{s,pre}/V_{s,exp} = 1.27$). It should be pointed out that Kanakubo's model [14,31] was developed based on a set of deep beam shear tests ($a/d \leq 1.8$), and some assumptions, such as the evaluation of μ_t and φ, are not suitable for the slender beams used in this research.

4.6. Modified truss-strut model and simplified shear strength prediction equation

By comparing the existing shear strength prediction models with test data, it can be found that the truss-strut model [25] not only provides a relatively accurate estimation of the ultimate shear-carrying capacity (V_u) but also predicts V_c and V_s well, demonstrating its ability to reflect the fundamental shear transfer mechanism in R/ECC beams. By incorporating the experimental results from this study, the shear test database of steel-reinforced ECC beams collected by [25] can be further expanded. Then, a modification can be made on the tensile stress reduction factor (μ_t) and characteristic inclined angle (φ) through nonlinear regression analysis, as follows:

$$\mu_t = 2.6\left(\frac{a}{d}\right)^{-3.0} \leq 1.0 \tag{3}$$

$$\varphi = 47.7 - 7.5\left(\frac{a}{d}\right) - 3237.7\rho_t + 1683.7\rho_t\left(\frac{a}{d}\right) \tag{4}$$

The average $V_{c,pre}/V_{c,exp}$ and $V_{s,pre}/V_{s,exp}$ are found to be 1.17 and 0.96, respectively, with coefficients of variation of 0.19 and 0.33. Fig. 29 compares the experimental ultimate shear strength of R/ECC beams in the expanded shear test database with the predicted values from various models. In terms of predicting the total shear-carrying capacity (V_u), T/CECS 1212–2022 [30], Hou and Xu's model [29,34] and the modified truss-strut model all provide satisfactory estimations (average $v_{u,pre}/v_{u,exp}$ = 1.00–1.02, CoV. = 0.14–0.17). However, these models appear in relative complicated forms and not user-friendly for the shear design of R/ECC beams. To simplify it, an empirical equation for predicting V_u in R/ECC beams is proposed:

$$V_u = \left(\frac{k_1\rho_l + k_2}{\frac{a}{d} + k_3} f'_c + k_4\rho_t f_{yv}\right)bd \tag{5}$$

where k_1, k_2, k_3 and k_4 are undetermined coefficients. Based on the expanded shear test database, these coefficients can be derived through nonlinear regression analysis, yielding the simplified shear strength equation:

$$V_u = \left(\frac{3.1\rho_l + 0.14}{a/d + 0.25} f'_c + \rho_t f_{yv}\right)bd \tag{6}$$

with a coefficient of determination (R^2) of 0.92. It is important to note that the value of $k_4 = 1.0$ is derived from nonlinear regression analysis of the test data, rather than assuming an inclined shear crack angle of 45°. Although the equation is presented in two parts, the annotation behind is not dividing V_u into V_c and V_s. Instead, the first part, $\frac{k_1\rho_l + k_2}{\frac{a}{d} + k_3} f'_c bd$, represents the V_u of R/ECC beams without stirrups, while the second part, $k_4\rho_t f_{yv} bd$, represents the increase in V_u when stirrups are added. Different from normal shear strength equations for R/ECC beams [14,25,29–31,34,44], such empirical model does not treat the fiber's contribution as a separate item, but incorporates it as part of V_c. The comparison is also made between the simplified model and test results in Fig. 29(f), showing accurate prediction on the total shear-carrying capacity of R/ECC beams (average $v_{u,pre}/v_{u,exp}$ = 1.00, CoV. = 0.10).

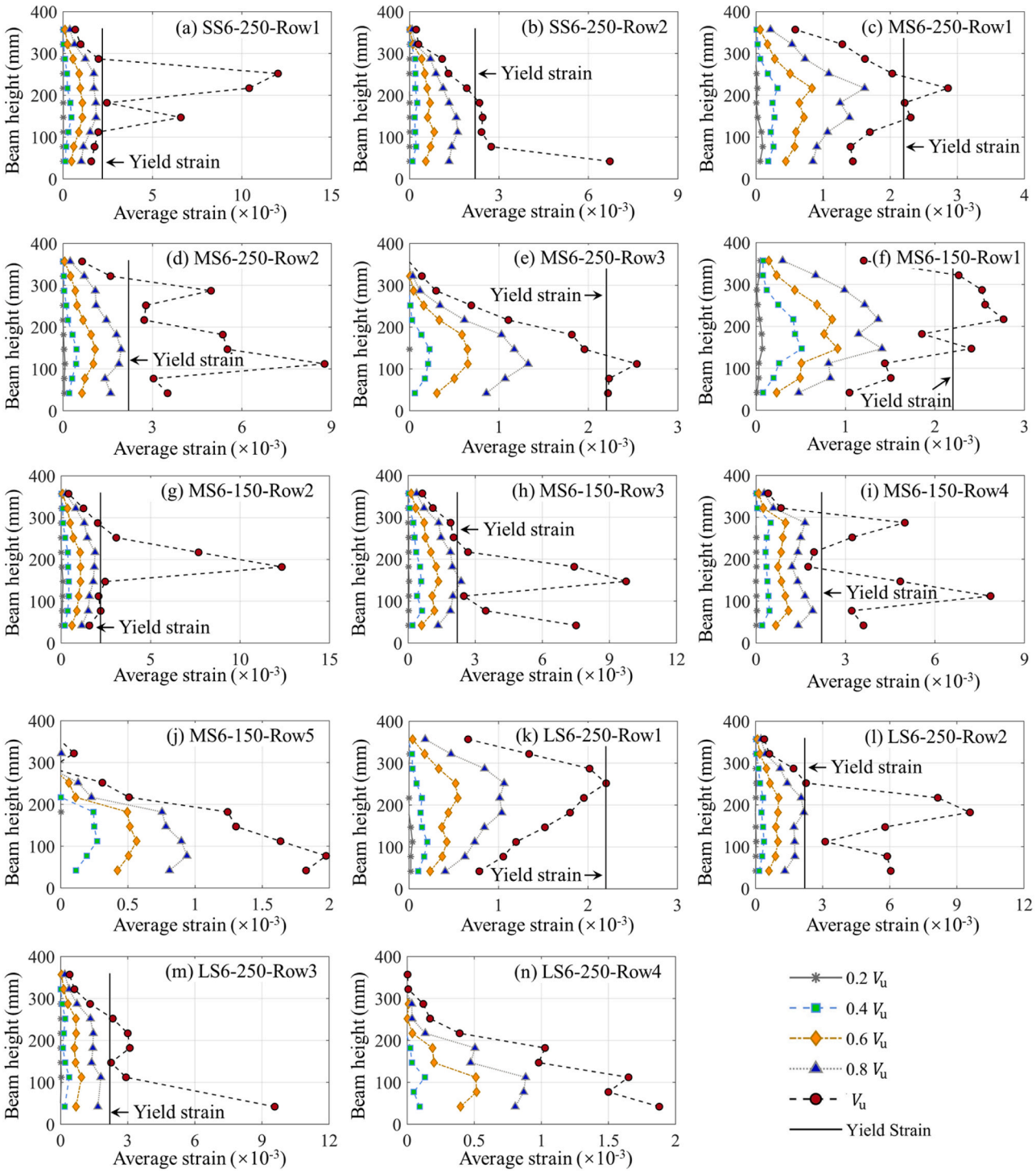

Fig. 25. Strain distribution along stirrups for selected beams (the stirrup position is marked in Fig. 17).

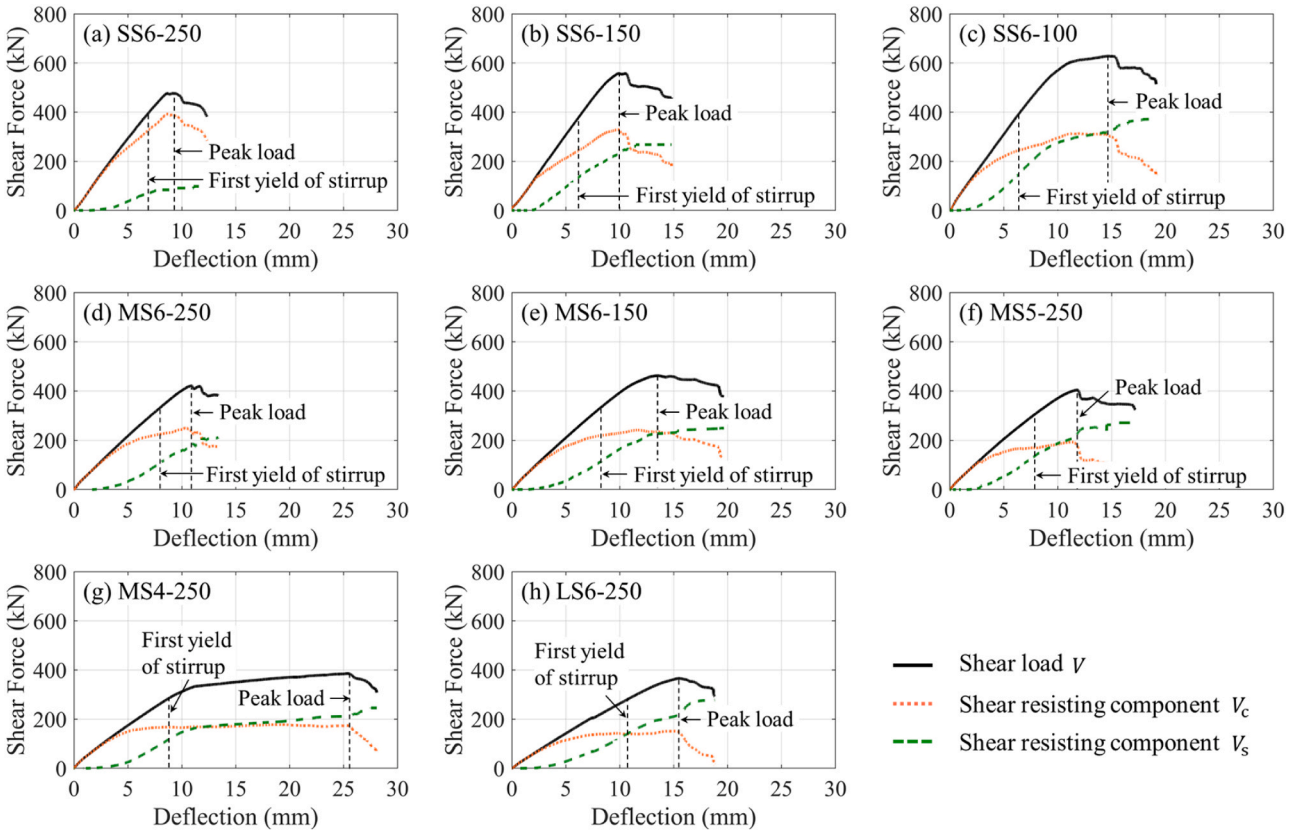

Fig. 26. Variations in V_c and V_s for the beams: (a) SS6–250; (b) SS6–150; (c) SS6–100; (d) MS6–250; (e) MS6–150; (f) MS5–250; (g) MS4–250; (h) LS6–250.

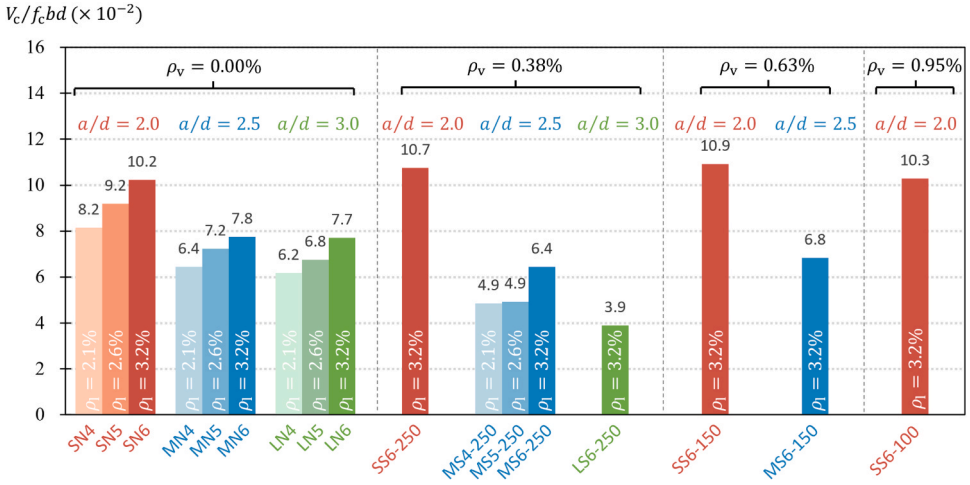

Fig. 27. Comparison of V_c at the peak load of beams failing in shear.

Nevertheless, the mechanics-based truss-strut model is still recommended with priority and the empirical shear strength equation should be validated through additional testing.

5. Conclusion

In this study, a distributed strain gauging scheme was employed to measure the continuous strain distribution along both the stirrups and longitudinal reinforcement in shear-critical R/ECC beams. By capturing stirrup strain precisely at the critical shear cracking path, the shear-resisting contributions from the stirrups (V_s) and the ECC matrix (V_c) were accurately quantified. Finally, several existing shear strength prediction equations for R/ECC beams were critically evaluated, and a modified truss-strut model was proposed. The main conclusions are drawn as follows:

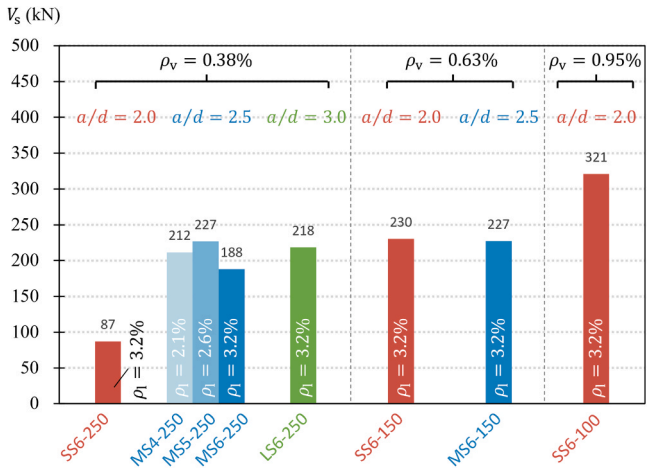

Fig. 28. Comparison of V_s at the peak load of beams failing in shear.

- The longitudinal reinforcement's strain distribution did not adhere to the moment diagram after shear cracking. A tension-shifting effect arose and caused increased anchoring force in tensile rebars near the beam ends.
- The stirrup strain varied along the beam's height, consistently exhibiting the highest values where the shear crack intersected the stirrups. The stirrups intersected by the critical shear crack did not always yield when the beam's shear-carrying capacity was reached.
- The shear load in R/ECC beams was solely resisted by V_c before shear cracks developed. After crack formation, V_s was gradually activated, and V_c continued increasing until approaching the beam's shear strength. However, V_c, V_s and V_u did not always reach their peak resistance simultaneously.
- Increasing the shear span-to-depth ratio from 2.0 to 3.0 resulted in a 25 % reduction in V_c (in beams without stirrups) and up to a 64 % reduction (in beams with stirrups). A negative combined effect between V_c and V_s was observed in slender beams ($a/d \geq 2.5$), where beams with higher stirrup ratios exhibited lower V_c.
- All five existing shear strength prediction models for R/ECC beams overestimate V_c to a certain extent (25 %~136 %). Most of them assume a critical shear crack angle of 45°, leading to underestimations of V_s by 27~36 %. The proposed modified truss-stut model not only accurately predicts the shear strength of R/ECC beams (average $v_{u,pre}/v_{u,exp} = 1.01$, CoV. = 0.16), but also effectively reflects the fundamental shear transfer mechanism in terms of truss action and strut action. To simplify the shear design of R/ECC beams, an empirical shear strength prediction equation is proposed (average $v_{u,pre}/v_{u,exp} = 1.00$, CoV. = 0.10). However, it should be validated by more shear tests in the future.

Table 4
Tested stirrup stress along the critical shear crack when reaching the beams' shear strength.

Specimen ID	Tested stirrup stress along the critical shear crack at the peak load (MPa)								Average stress (MPa)	k
	First row		Second row		Third row		Fourth row			
	Front	Back	Front	Back	Front	Back	Front	Back		
MS6–250	268	246	440	440	440	390	–	–	370.6	0.84
MS5–250	380	375	440	440	440	440	–	–	419.2	0.95
MS4–250	440	346	440	440	355	440	–	–	410.1	0.93
MS6–150	440	440	449	440	440	440	–	–	441.5	1.00
SS6–250	440	477	–	–	–	–	–	–	458.3	1.04
SS6–150	–	–	440	440	440	476	416	318	421.8	0.96
SS6–100	405	405	448	440	440	440	484	449	438.8	1.00
LS6–250	292	245	440	440	440	440	–	–	382.8	0.87

Table 5
Existing shear strength prediction equations for R/ECC beams.

T/CECS 1212–2022 [30]	**Kanakubo's model** [14, 31]	**Truss-strut model** [25]	**JSCE 08** [44]	**Hou and Xu's model** [29,34]
$V_u = V_c + V_s$ $V_c = \alpha(1-\beta)\mu_c f_c' bd + \mu_t f_{tu} bz\cot\varphi$ $V_s = \rho_t f_{yv} bz\cot\varphi$ $\alpha = 0.5\sqrt{(0.9\lambda)^2 + 2\sin(2\varphi) - \sin^2(2\varphi)} - 0.45\lambda$ $\beta = \frac{\rho_t f_{yv} + \mu_t f_{tu}}{\mu_c f_c' \eta_t \sin^2\varphi}\cos(\varphi-\theta) \leq 1$ $\tan\theta = \frac{\sqrt{(0.9\lambda)^2 + 2\sin(2\varphi) - \sin^2(2\varphi)} - 0.9\lambda}{\sin(2\varphi)}$ $\mu_c = 0.75 - \frac{f_c'}{170} \geq 0.4$ $\mu_t = 0.5$ $z = 0.9d$ $\lambda = \frac{a}{d}$ $\varphi = 45°$ $\eta_t = 1 - \frac{b}{4z}$	$V_u = V_c + V_s$ $V_c = \frac{\tan\theta(1-\beta)\mu_c f_c' bD}{2} + bz\mu_t f_{tu}\cot\varphi$ $V_s = \rho_t f_{yv} bz\cot\varphi$ $\tan\theta = \sqrt{(L/D)^2 + 1} - (L/D)$ $\beta = \frac{(1+\cot^2\varphi)\rho_t f_{yv}}{\mu_c f_c'}$ $\cot\varphi = \min\left\{\begin{matrix} 2.0 \\ \frac{z}{D\tan\theta} \\ \sqrt{\frac{\mu_c f_c'}{\rho_t f_{yv}} - 1} \end{matrix}\right.$ $\mu_c = 1.7 f_c'^{-0.333}$ $\mu_t = 0.5$ $z = \frac{d}{1.15}$	$V_u = V_c + V_s$ If $\rho_t f_{yv} \leq \frac{\mu_c f_c' - \mu_t f_{tu}\cot^2\varphi}{1+\cot^2\varphi}$: $V_c = (1-\beta)\mu_c f_c' bx_0 + bj_t\mu_t f_{tu}\cot\varphi$ $V_s = \rho_t f_{yv} bj_t\cot\varphi$ $\beta = \frac{(1+\cot^2\varphi)\rho_t f_{yv} + \mu_t f_{tu}\cot^2\varphi}{\mu_c f_c'}$ $x_0 = \min(x_{plate}, \frac{\sqrt{L^2+D^2}-L}{2})$ $\mu_c = 0.6(1 - \frac{f_c'}{250})$ $\mu_t = 1.9(\frac{a}{d})^{-2.3}$ $\varphi = 43.8 - 6.1(\frac{a}{d}) - 3771.9\rho_t + 2047.5\rho_t(\frac{a}{d})$ If $\rho_t f_{yv} > \frac{\mu_c f_c' - \mu_t f_{tu}\cot^2\varphi}{1+\cot^2\varphi}$: $V_c = bj_t\mu_t f_{tu}\cot\varphi$ $V_s = \frac{bj_t\cot\varphi(\mu_c f_c' - \mu_t f_{tu}\cot^2\varphi)}{1+\cot^2\varphi}$	$V_u = V_c + V_s$ $V_c = \beta_d\beta_p f_{vc} bd + \frac{f_{ty} bz}{\tan\beta_u}$ $V_s = \rho_t f_{yv} bz$ $\beta_d = \sqrt[4]{\frac{1000}{d}} \leq 1.5$ $\beta_p = \sqrt[3]{100\rho_l} \leq 1.5$ $\beta_u = 45°$ $f_{vc} = 0.14\sqrt[3]{f_c'} \leq 0.5$ $z = \frac{d}{1.15}$	For beams without stirrup : $V_u = V_c = v_m bd$ For beams with stirrup : $V_u = V_c + V_s$ $V_c = [v_m - 1.12\rho_t(v_m)^{0.25}]bd$ $V_s = \rho_t f_{yv} bd$ When $\frac{a}{d} \geq 2.5$: $v_m = 0.29\eta A + 5.2B + 2.02\eta AB$ When $\frac{a}{d} < 2.5$: $v_m = \frac{d}{a}(1.03A + 16.25B) + 0.8 f_{sp} B$ $f_{sp} = 0.29(f_c')^{\frac{2}{3}} + 0.28F + 0.11F(f_c')^{\frac{2}{3}}$ $A = f_{sp}^{\frac{2}{3}}$, $B = \left(\rho_l\frac{d}{a}\right)^{\frac{1}{3}}$ $\eta = (\frac{F}{0.3})^{\frac{2}{3}} \leq 1$ $F = (\frac{L_f}{D_f})V_f d_f$

Table 6
Comparison of shear strength components.

Specimen ID	Tested value			T/CECS 1212–2022 [30]			Kanakubo's model [14,31]			Truss-strut model [25]			JSCE 08 [44]			Hou and Xu's model [29,34]		
	$V_{c,exp}$ (kN)	$V_{s,exp}$ (kN)	$V_{u,exp}$ (kN)	$\frac{V_{c,pre}}{V_{c,exp}}$	$\frac{V_{s,pre}}{V_{s,exp}}$	$\frac{V_{u,pre}}{V_{u,exp}}$	$\frac{V_{c,pre}}{V_{c,exp}}$	$\frac{V_{s,pre}}{V_{s,exp}}$	$\frac{V_{u,pre}}{V_{u,exp}}$	$\frac{V_{c,pre}}{V_{c,exp}}$	$\frac{V_{s,pre}}{V_{s,exp}}$	$\frac{V_{u,pre}}{V_{u,exp}}$	$\frac{V_{c,pre}}{V_{c,exp}}$	$\frac{V_{s,pre}}{V_{s,exp}}$	$\frac{V_{u,pre}}{V_{u,exp}}$	$\frac{V_{c,pre}}{V_{c,exp}}$	$\frac{V_{s,pre}}{V_{s,exp}}$	$\frac{V_{u,pre}}{V_{u,exp}}$
MN6	289.5	–	289.5	1.20	–	1.20	2.38	–	2.38	1.30	–	1.30	1.49	–	1.49	1.08	–	1.08
MN5	295.3	–	295.3	1.22	–	1.22	2.42	–	2.42	1.34	–	1.34	1.47	–	1.47	1.04	–	1.04
MN4	286.4	–	286.4	1.30	–	1.30	2.52	–	2.52	1.43	–	1.43	1.58	–	1.58	1.05	–	1.05
LN6	302.0	–	302.0	1.07	–	1.07	2.11	–	2.11	1.03	–	1.03	1.43	–	1.43	1.01	–	1.01
LN5	261.4	–	261.4	1.25	–	1.25	2.46	–	2.46	1.19	–	1.19	1.59	–	1.59	1.11	–	1.11
LN4	302.4	–	302.4	1.21	–	1.21	2.29	–	2.29	1.15	–	1.15	1.56	–	1.56	0.98	–	0.98
SN6	377.9	–	377.9	0.97	–	0.97	1.94	–	1.94	1.29	–	1.29	1.02	–	1.02	1.13	–	1.13
SN5	344.9	–	344.9	1.07	–	1.07	2.15	–	2.15	1.43	–	1.43	1.26	–	1.26	1.19	–	1.19
SN4	295.3	–	295.3	1.21	–	1.21	2.39	–	2.39	1.60	–	1.60	1.32	–	1.32	1.31	–	1.31
MS6–250	233.2	188.2	421.4	1.33	0.53	0.97	2.48	1.02	1.83	1.28	0.77	1.05	1.78	0.51	1.21	1.33	0.59	1.00
MS5–250	177.3	226.8	404.1	1.77	0.44	1.02	3.29	0.85	1.92	1.68	0.64	1.10	2.25	0.42	1.23	1.70	0.49	1.02
MS4–250	173.9	211.7	385.5	1.77	0.47	1.06	3.29	0.91	1.98	1.69	0.68	1.14	2.24	0.45	1.26	1.69	0.52	1.05
MS6–150	235.2	227.2	462.4	1.20	0.73	0.97	2.09	1.40	1.76	1.07	0.93	1.00	1.72	0.70	1.22	1.39	0.81	1.10
LS6–250	147.3	218.4	365.7	2.02	0.46	1.09	3.78	0.88	2.05	1.64	0.64	1.04	2.51	0.44	1.27	2.24	0.51	1.20
SS6–250	389.9	87.2	477.0	0.87	1.14	0.92	1.65	2.21	1.75	1.07	1.71	1.19	1.18	1.10	1.17	1.23	1.27	1.23
SS6–150	327.6	230.3	557.9	0.87	0.72	0.81	1.50	1.39	1.45	0.96	1.04	0.99	1.14	0.69	0.96	1.39	0.80	1.15
SS6–100	307.2	320.8	628.0	0.86	0.78	0.82	1.37	1.50	1.44	0.88	1.09	0.99	1.18	0.75	0.96	1.52	0.86	1.18
Aver.	–	–	–	**1.25**	**0.66**	**1.07**	**2.36**	**1.27**	**2.05**	**1.30**	**0.94**	**1.19**	**1.57**	**0.64**	**1.30**	**1.32**	**0.73**	**1.11**
CoV.	–	–	–	**0.26**	**0.34**	**0.13**	**0.26**	**0.34**	**0.16**	**0.19**	**0.36**	**0.15**	**0.26**	**0.34**	**0.15**	**0.24**	**0.34**	**0.08**

Notes: Aver. represents the mean value (μ), where $\mu = \frac{1}{n}\sum_{i=1}^{n} x_i$; CoV. represents the coefficient of variation (c_v), where $c_v = \frac{1}{\mu}\sqrt{\frac{1}{n}\sum_{i=1}^{n}(x_i - \mu)^2}$; $V_{c,exp}$, $V_{s,exp}$ and $V_{u,exp}$ is the measured shear strength components; $V_{c,pre}$, $V_{s,pre}$ and $V_{u,pre}$ is the predicted shear strength components.

Notation

a = shear span length

A_s = cross-section area of the stirrup leg

b = beam width

C = resultant compressive force of intact matrix in shear compression zone

d = effective depth of beam

d_f = fiber-matrix bond factor (0.5 for round fiber, 0.75 for crimped fiber, and 1.0 for indented fiber)

D = depth of beam

D_f = diameter of fiber

f_c' = compressive strength of ECC

f_{sp} = splitting tensile strength of ECC

f_{ty} = nominal tensile yield strength of ECC

f_{tu} = tensile strength of ECC

f_{vc} = compressive strength factor of ECC

$f_{v,aver}$ = average stress of stirrups at the critical shear cracking path

f_{yv} = yielding strength of stirrup

F = fiber factor

j_t = distance between top and bottom flexural reinforcement

k = efficiency factor of stirrups

L = beam span length

L_c = horizontal projection length of the critical shear crack

L_f = length of fiber

n = total number of transverse rebars

s = stirrup spacing distance

T = resultant tensile force of longitudinal tensile reinforcement

v = nominal shear stress

V = shear force

V_a = shear force carried by intact ECC in shear compression zone

V_c = shear-resisting contribution from ECC matrix

V_{cd} = dowel force of longitudinal tensile reinforcement

V_{cr} = initial shear cracking load

V_f = volume fraction of fiber

v_m = nominal shear strength for beams without stirrups

V_s = shear-resisting contribution from stirrups

V_{si} = force of ith stirrup leg

v_u = nominal shear strength

V_u = total shear-carrying capacity

x_0 = effective bearing length of hydrostatic nodes

x_{plate} = length of bearing plate

z = distance from tensile to compressive resultant force

α = arch action factor

β = proportion of truss action in total shear-carrying capacity

β_d = size effect factor

β_p = longitudinal reinforcement factor

β_u = inclined angle of the critical shear crack

ε_{tu} = ultimate tensile strain of ECC

η = fiber modification factor

η_t = stirrup confinement factor

θ = inclined angle of ECC arch

λ = shear span-to-effective depth ratio

μ_c = compressive strength reduction factor of ECC

μ_t = tensile strength reduction factor of ECC

ρ_l = longitudinal tensile reinforcement ratio

ρ_t = stirrup ratio

σ_{fiber} = fiber bridging stress along diagonal shear crack

φ = characteristic inclined angle of compressive struts in truss action

Author Statement

We, the authors of the manuscript titled "Understanding the Shear-Resisting Mechanism in Reinforced Engineered Cementitious Composite (ECC) Beams Using Distributed Strain Measurements", declare that this work is original and has not been submitted or published elsewhere. Each author has significantly contributed to the research, analysis, and preparation of the manuscript.

The research presented in this paper was focusing on the shear behavior of reinforced engineered cementitious composites (ECC) beams. The experiments, data analysis, and interpretation were carried out with rigor and academic integrity, ensuring the reliability and reproducibility of the findings.

All authors have reviewed and approved the final version of the manuscript, and agree to be accountable for the content. There are no conflicts of interest to disclose, and all necessary funding sources and

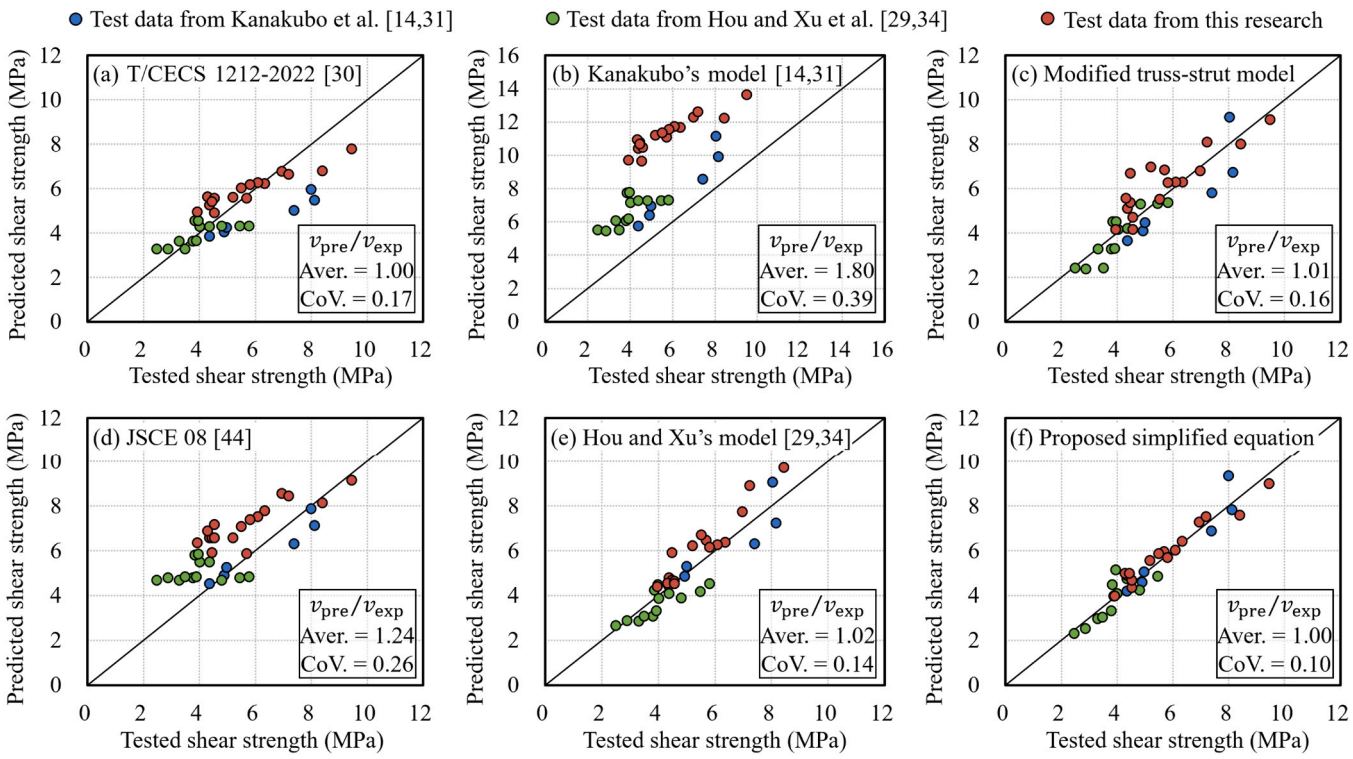

Fig. 29. Comparison between tested ultimate shear strength and the predicted value based on: (a) T/CECS 1212–2022 [30]; (b) Kanakubo's model [14,31]; (c) modified truss-strut model;(d) JSCE 08 [44]; (e) Hou and Xu's model [29,34]; (f) proposed simplified empirical equation.

acknowledgments have been properly cited in the manuscript. We are committed to maintaining high ethical standards in research and publication.

CRediT authorship contribution statement

Mladena Luković: Writing – review & editing, Supervision, Conceptualization. **Jinlong Pan:** Writing – review & editing, Supervision, Funding acquisition, Conceptualization. **Dawei Gu:** Writing – original draft, Methodology, Investigation, Funding acquisition, Conceptualization.

Declaration of Competing Interest

The authors declare that they have no known competing financial interests or personal relationships that could have appeared to influence the work reported in this paper.

Acknowledgements

The work is financially supported by the Natural Science Foundation of Jiangsu Province (BK20230860) and National Natural Science Foundation of China (No. 51778131).

Data Availability

Data will be made available on request.

References

[1] Baradaran Shoraka M, Yang TY, Elwood KJ. Seismic loss estimation of non-ductile reinforced concrete buildings. Earthq Eng Struct Dyn 2013;42(2):297–310. https://doi.org/10.1002/eqe.2213.
[2] Li VC, Leung CKY. Steady-state and multiple cracking of short random fiber composites. J Eng Mech 1992;118:2246–64. https://doi.org/10.1061/(asce)0733-9399(1992)118:11(2246).
[3] Yang EH, Wang S, Yang Y, Li VC. Fiber-bridging constitutive law of engineered cementitious composites. J Adv Concr Technol 2008;6:181–93. https://doi.org/10.3151/jact.6.181.
[4] Li VC. Engineered cementitious composites (ECC) – tailored composites through micromechanical modeling. Can Soc Civ Eng 1997:1–38.
[5] Yu K, Li L, Yu J, Wang Y, Ye J, Xu Q. Direct tensile properties of engineered cementitious composites: a review. Constr Build Mater 2018;165:346–62. https://doi.org/10.1016/j.conbuildmat.2017.12.124.
[6] Jun P, Mechtcherine V. Behaviour of strain-hardening cement-based composites (SHCC) under monotonic and cyclic tensile loading: Part 1 - experimental investigations. Cem Concr Compos 2010;32(10):801–9. https://doi.org/10.1016/j.cemconcomp.2010.07.019.
[7] Yang J, Jiang L, Guo H, Yao G. Stress mechanism and energy dissipation performance optimization of prefabricated ECC/RC combined shear walls under low cyclic loading. Buildings 2023;13(3):772. https://doi.org/10.3390/buildings13030772.
[8] Tian J, Wu X, Tan X, Wang W, Hu S, Du Y, et al. Experimental study and analysis model of flexural synergistic effect of reinforced concrete beams strengthened with ECC. Constr Build Mater 2022;352:128987. https://doi.org/10.1016/j.conbuildmat.2022.128987.
[9] Tian J, Wu X, Zuo Y, Yuan J, Wang W. Interface behaviors between smart-functional ECC and steel rebar under coupling effect of sustained load and chloride ion erosion: corrosion resistance, mechanical and self-sensing properties. Constr Build Mater 2024;438:137205. https://doi.org/10.1016/j.conbuildmat.2024.137205.
[10] Xu L, Pan J, Cai J. Seismic performance of precast RC and RC/ECC composite columns with grouted sleeve connections. Eng Struct 2019;188:104–10. https://doi.org/10.1016/j.engstruct.2019.03.022.
[11] Cai J, Pan J, Xu L, Li G, Ma T. Mechanical behavior of RC and ECC/RC composite frames under reversed cyclic loading. J Build Eng 2021;35:102036. https://doi.org/10.1016/j.jobe.2020.102036.
[12] Li VC, Mishra DK, Naaman AE, Wight JK, LaFave JM, Wu HC, et al. On the shear behavior of engineered cementitious composites. Adv Cem Based Mater 1994;1:142–9. https://doi.org/10.1016/1065-7355(94)90045-0.
[13] van Zijl GPAG. Improved mechanical performance: Shear behaviour of strain-hardening cement-based composites (SHCC). Cem Concr Res 2007;37:1241–7. https://doi.org/10.1016/j.cemconres.2007.04.009.
[14] Kanakubo T., Shimizu K., Nagai S., Kanda T. Shear transmission on crack surface of ECC. 7th Int. Conf. Fract. Mech. Concr. Concr. Struct., Jeju, Korea: 2010, p. 1623–1630.
[15] Wu C, Leung CKY, Li VC. Derivation of crack bridging stresses in engineered cementitious composites under combined opening and shear displacements. Cem Concr Res 2018;107:253–63. https://doi.org/10.1016/j.cemconres.2018.02.027.
[16] Kanda T., Nagai S., Maruta M., Yamamoto Y. New high-rise R/C structure using ECC coupling beams. 2nd Int. RILEM Conf. Strain Hardening Cem. Compos., Rio de Janeiro, Brazil: 2011, p. 289–296.

[17] Zhang R, Matsumoto K, Hirata T, Ishizeki Y, Niwa J. Application of PP-ECC in beam-column joint connections of rigid-framed railway bridges to reduce transverse reinforcements. Eng Struct 2015;86:146–56. https://doi.org/10.1016/j.engstruct.2015.01.005.
[18] Hung CC, Hsiao HJ, Shao Y, Yen CH. A comparative study on the seismic performance of RC beam-column joints retrofitted by ECC, FRP, and concrete jacketing methods. J Build Eng 2023;64:105691. https://doi.org/10.1016/j.jobe.2022.105691.
[19] Yang X, Xu L, Pan J. Mechanical behavior of full-scale composite steel plate shear wall restrained by ECC panels. J Build Eng 2021;44:102864. https://doi.org/10.1016/j.jobe.2021.102864.
[20] Ye B, Wang H, Ma Y, Pan P. Seismic performance of flexure-dominated reinforced-engineered cementitious composites coupled shear wall. Eng Struct 2022;272:114992. https://doi.org/10.1016/j.engstruct.2022.114992.
[21] Hassan A, Baraghith AT, Atta AM, El-Shafiey TF. Retrofitting of shear-damaged RC T-beams using U-shaped SHCC jacket. Eng Struct 2021;245:112892. https://doi.org/10.1016/j.engstruct.2021.112892.
[22] Wei J, Wu C, Chen Y, Leung CKY. Shear strengthening of reinforced concrete beams with high strength strain-hardening cementitious composites (HS-SHCC). Mater Struct Constr 2020;53:102. https://doi.org/10.1617/s11527-020-01537-1.
[23] Gu D., Pan J., He J. Shear behavior of ECC and concrete/ECC composite beams reinforced with BFRP bars. 6th Asia-Pacific Conf. FRP Struct, Singapore: 2017.
[24] Gu D, Pan J, Mustafa S, Huang Y, Luković M. Shear transfer mechanism in reinforced engineered cementitious composite (ECC) beams: quantification of Vs and Vc. Eng Struct 2022;261:114282. https://doi.org/10.1016/j.engstruct.2022.114282.
[25] Gu D, Pan J, Luković M, He J. Experimental and analytical study on shear behavior of strain-hardening cementitious composite beams reinforced with fiber-reinforced polymer bars. Struct Concr 2022;23:1080–99. https://doi.org/10.1002/suco.202100544.
[26] Paegle I, Fischer G. Phenomenological interpretation of the shear behavior of reinforced engineered cementitious composite beams. Cem Concr Compos 2016;73:213–25. https://doi.org/10.1016/j.cemconcomp.2016.07.018.
[27] Shimizu K, Kanakubo T, Kanda T, Saotoru N. Shear behavior of steel reinforced PVA-ECC beams. 13th World Conf. Earthq. Eng. Vancouver, Canada: WCEE; 2004. https://doi.org/10.5459/bnzsee.38.1.41-49.
[28] Xu S, Hou L, Zhang X. Flexural and shear behaviors of reinforced ultrahigh toughness cementitious composite beams without web reinforcement under concentrated load. Eng Struct 2012;39:176–86. https://doi.org/10.1016/j.engstruct.2012.01.011.
[29] Xu S, Hou L, Zhang X. Shear behavior of reinforced ultrahigh toughness cementitious composite beams without transverse reinforcement. J Mater Civ Eng 2012;24:1283–94. https://doi.org/10.1061/(asce)mt.1943-5533.0000505.
[30] CECS (China Association for Engineering Construction Standardization). Technical specification for strain-hardening cementitious composites structures (T/CECS 1212-2022). Beijing: China Planning Press; 2022.
[31] Kanakubo T., Shimizu K., Kanda T., Nagai S. Evaluation of bending and shear capacities of HPFRCC members toward the structural application. Hokkaido Univ. COE Work. High Perform. Fiber Reinf. Compos. Sustain. Infrastruct. Syst. – Mater. Model. Struct. Des. Appl., Sapporo, Japan: 2007, p. 1–10.
[32] Vasillaq X. Investigating the shear characteristics of high performance fiber reinforced concrete. University of Toronto; 2003.
[33] Emmanuel KA, Michael NP, Darwin D. Shear cracking and stirrup effectiveness of lightly reinforced concrete beams. Lawrence, Kansas: University of Kansas; 1980.
[34] Hou L, Xu S, Zhang X, Chen D. Shear behaviors of reinforced ultrahigh toughness cementitious composite slender beams with stirrups. J Mater Civ Eng 2014;26:466–75. https://doi.org/10.1061/(asce)mt.1943-5533.0000833.
[35] Li W, Leung CKY. Shear span–depth ratio effect on behavior of RC beam shear strengthened with full-wrapping FRP strip. J Compos Constr 2016;20(3):04015067. https://doi.org/10.1061/(asce)cc.1943-5614.0000627.
[36] Qin S, Dirar S, Yang J, Chan AHC, Elshafie M. CFRP shear strengthening of reinforced-concrete T-beams with corroded shear links. J Compos Constr 2015;19(5):04014081. https://doi.org/10.1061/(asce)cc.1943-5614.0000548.
[37] Hu B, Wu YF. Effect of shear span-to-depth ratio on shear strength components of RC beams. Eng Struct 2018;168:770–83. https://doi.org/10.1016/j.engstruct.2018.05.017.
[38] Hu B, Wu YF. Quantification of shear cracking in reinforced concrete beams. Eng Struct 2017;147:666–78. https://doi.org/10.1016/j.engstruct.2017.06.035.
[39] Wu Y, Hu B. Shear strength components in reinforced concrete members. J Struct Eng 2017;143:1–16. https://doi.org/10.1061/(asce)st.1943-541x.0001832.
[40] Poldon JJ, Hoult NA, Bentz EC. Understanding reinforcement behavior using distributed measurements of shear tests. Acids Struct J 2021;118:255–66. https://doi.org/10.14359/51730537.
[41] Poldon JJ, Hoult NA, Bentz EC. Distributed sensing in large reinforced concrete shear test. Acids Struct J 2019;116:235–45. https://doi.org/10.14359/51716765.
[42] Zhang Z, Yuvaraj A, Di J, Qian S. Matrix design of light weight, high strength, high ductility ECC. Constr Build Mater 2019;210:188–97. https://doi.org/10.1016/j.conbuildmat.2019.03.159.
[43] Ministry MIIT. of Industry and Information Technology of the People's Republic of China). Standard test method for the mechanical properties of ductile fiber reinforced cementitious composite (JC/T 2461-2018). Beijing, China: Building Industry Press; 2018.
[44] JSCE (Japan Society of Civil Engineers). Recommendations for design and construction of high performance fiber reinforced cement composites with multiple fine cracks (HPFRCC). Tokyo: 2008.
[45] ASTM International. Standard test method for compressive strength of cylindrical concrete specimens (C39/C39M-16). Pennsylvania: 2016.
[46] Lu C, Pang Z, Chu H, Leung CKY. Experimental and numerical investigation on the long-term performance of engineered cementitious composites (ECC) with high-volume fly ash and domestic polyvinyl alcohol (PVA) fibers. J Build Eng 2023;70:106324. https://doi.org/10.1016/j.jobe.2023.106324.
[47] Gu D, Pan J, Mustafa S, Huang Y, Luković M. Shear transfer mechanism in reinforced engineered cementitious composite (ECC) beams: quantification of Vs and Vc. Eng Struct 2022;261:114282. https://doi.org/10.1016/j.engstruct.2022.114282.
[48] Gehri N, Mata-Falcón J, Kaufmann W. Automated crack detection and measurement based on digital image correlation. Constr Build Mater 2020;256:119383. https://doi.org/10.1016/j.conbuildmat.2020.119383.
[49] Gehri N, Mata-Falcón J, Kaufmann W. Refined extraction of crack characteristics in large-scale concrete experiments based on digital image correlation. Eng Struct 2022;251:113486. https://doi.org/10.1016/j.engstruct.2021.113486.
[50] Park R, Paulay T. Reinforced Concrete Structures. Hoboken, NJ: John Wiley & Sons; 1975.
[51] Schuler H, Meier F, Trost B. Influence of the tension shift effect on the force–displacement curve of reinforced concrete shear walls. Eng Struct 2023;274:115144. https://doi.org/10.1016/j.engstruct.2022.115144.
[52] Bandelt MJ, Billington SL. Bond behavior of steel reinforcement in high-performance fiber-reinforced cementitious composite flexural members. Mater Struct Constr 2016;49:71–86. https://doi.org/10.1617/s11527-014-0475-4.
[53] Gu D, Mustafa S, Pan J, Luković M. Reinforcement-concrete bond in discrete modeling of structural concrete. Comput Civ Infrastruct Eng 2023;38:1324–45. https://doi.org/10.1111/mice.12937.
[54] ACI (American Concrete Institute). Building Code Requirements for Structural Concrete and Commentary (ACI 318-19). MI: Farmington Hills; 2019. https://doi.org/10.14359/51716937.
[55] Mak MWT, Lees JM. Arch action in reinforced concrete subjected to shear. Eng Struct 2023;274:115096. https://doi.org/10.1016/j.engstruct.2022.115096.
[56] Kim JH, Mander JB. Influence of transverse reinforcement on elastic shear stiffness of cracked concrete elements. Eng Struct 2007;29(8):1798–807. https://doi.org/10.1016/j.engstruct.2006.10.001.
[57] Kim JH, Mander JB. Theoretical shear strength of concrete columns due to transverse steel. J Struct Eng 2005;131(1):197–9. https://doi.org/10.1061/(asce)0733-9445(2005)131:1(197).
[58] Laskar A, Hsu T, Mo YL. Shear strengths of prestressed concrete beams part 1: experiments and shear design equations. Acids Struct J 2010;107(3):330–9.
[59] Gu D, Xu H, Huang Y, Zhu Y, Pan J, Luković M. Shear crack kinematics in reinforced engineered cementitious composite (ECC) beams. Case Stud Constr Mater 2024;21:e03587. https://doi.org/10.1016/j.cscm.2024.e03587.